Defect Prediction in Axisymmetric Cold Forging - A Finite Element Analysis

By

Saurabh Gupta

DEPARTMENT OF MECHANICAL ENGINEERING

Indian Institute of Technology Kanpur

FEBRUARY, 2002

Defect Prediction in Axisymmetric Cold Forging - A Finite Element Analysis

A Thesis Submitted
In Partial Fulfillment of the Requirements
for the Degree of
Master of Technology

by

SAURABH GUPTA

to the
DEPARTMENT OF MECHANICAL ENGINEERING
INDIAN INSTITUTE OF TECHNOLOGY KANPUR
FEBRUARY, 2002

CERTIFICATE

It is certified that the work contained in the thesis entitled *"Defect Prediction in Axisymmetric Cold Forging - A Finite Element Analysis"*, by *Saurabh Gupta*, has been carried out under our supervision and that this work has not been submitted elsewhere for a degree.

Dr. P.M. Dixit
Dept. of Mechanical Engineering and
I.I.T Kanpur

Dr. N.V.Reddy
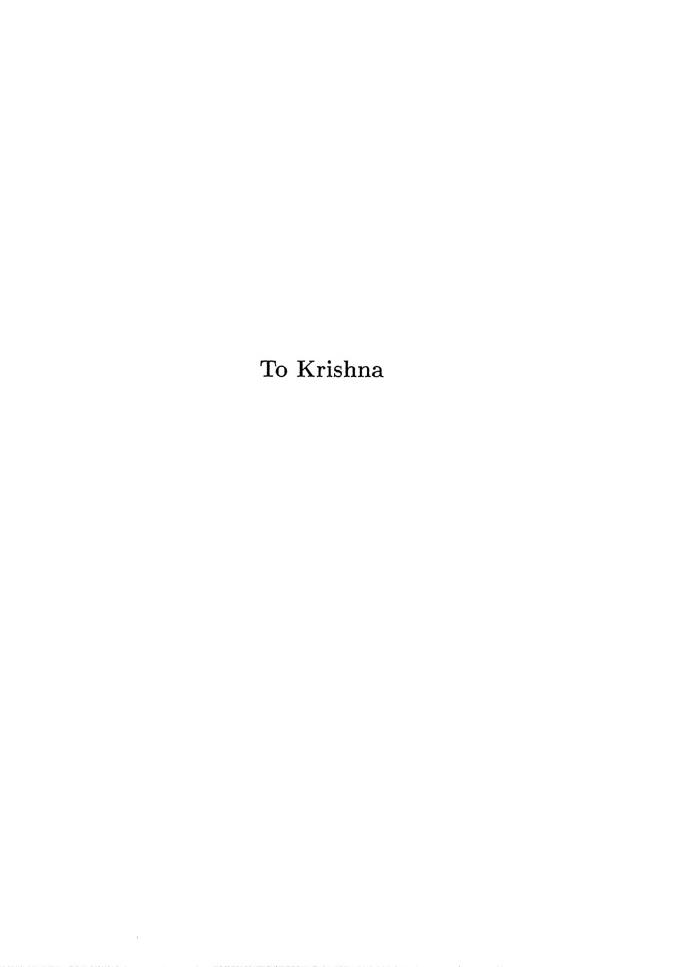Dept. of Mechanical Engineering
I.I.T. Kanpur

FEBRUARY, 2002

Acknowledgements

I wish to place on records my deep sense of gratitude and indebtedness to Dr. N. V. Reddy and Dr. P. M. Dixit for their expert guidance, valuable suggestions, personal encouragement and generous help during the course of my thesis work.

I am thankful to Karella, Kuldeep, Subodh and Bandaru for providing friendly environment during my stay in the FEAL. Sincere thanks are due to Poshan, Deshraj and other friends with whom I enjoyed the life at IITKanpur.

Saurabh Gupta

To Krishna

Abstract

In this work, an axisymmetric large deformation elasto-plastic finite element code for determination of damage in cold forging process is developed. For typical values of input variables, the damage, hydrostatic stress, circumferential stress and axial stress distributions are studied. A detailed parametric study of damage is carried out to show the effects of the coefficient of friction at the die-work interface and the height to diameter ratio of the blank.

The Updated Lagrangian formulation, which is convenient for handling material and geometric non-linearities, is used. New incremental objective stress measure and logarithmic strain measure are used which allow the use of large incremental displacement. The forging process is a displacement-control problem. Therefore, to accelerate the convergence of the iterative solution scheme, arc length method is used in conjunction with the modified Newton Raphson iterative technique. The material is assumed to be elastic-plastic strain hardening and yielding according to the von Mises criterion. Coulomb's friction law is used to model the friction at the die-workpiece interface. To facilitate the application of friction boundary condition and also to reduce the computational time, the static condensation of the coefficient matrix is carried out. The inertial and body forces are neglected. A continuum damage mechanics criterion to model ductile fracture in metal forming is used for defect prediction.

The study shows that the micro-cracks first initiate along the die-workpiece interface region near to the free surface, then at the centre of the workpiece and proceed to the meridian surface. The fracture will appear first at the meridian surface since, here, the hydrostatic stress and axial stress are the minimum compressive and the circumferential stress is the maximum tensile. Thus, micro-cracks here can grow faster to a fracture. From the parametric study it is observed that at higher friction, micro-cracks initiation and meridian surface fracture occurrence take place at less reduction. Bulging is more severe when the friction at die work interface is higher. As compared with the case of height to diameter ratio equal to one, blanks with height to diameter ratio less than or greater than unity can sustain more reductions without micro-cracks and fracture. Further, with higher height to diameter ratio the chances of formation of a central cavity are more because of less compressive hydrostatic stress at the centre.

Contents

List of Figures

Nomenclature

a_1	Constant used in Dhar's model.
a_2	Constant used in Dhar's model.
$\{a\}$	Flow vector.
$[B_L]$	Linear strain displacement matrix.
$[B_N]$	Non-linear strain displacement matrix.
C_D	Constant used in Dhar's model.
C^E	Fourth order elasticity tensor.
C^E	Fourth order elastic-plastic tensor.
$[C^E]$	Elasticity matrix.
$[C^E]$	Elasto-plastic matrix.
D	Damage Variable.
$e,\ e_{ij}$	Green-Lagrange strain tensor, component.
E	Young's modulus.
$f(),\ F()$	Generic representation of functions.
F_r	Component of force in radial direction.
F_z	Component of force in axial direction.
f_i	Surface force component.
$\{f\}$	Global internal force vector.
$\boldsymbol{F},\ F_{ij}$	Deformation gradient tensor, component.
$[F]$	Matrix representation of Deformation gradient tensor.

$\{F_1\}$	External force vector corresponding to nodes of type 1.
$\{F_2\}$	External force vector corresponding to nodes of type 2.
$\{\widehat{F}\}$	Condensed form of global external force vector.
$\{F\}$	Global external force vector.
H	Height of the workpiece.
K	Hardening coefficient.
$[K]$	Stiffness matrix.
$[K_L]$	Linear part of stiffness matrix.
$[K_N]$	Non-linear part of stiffness matrix.
$[\widehat{K}]$	Condensed form of stiffness matrix.
t_r	Traction in radial direction.
t_z	Traction in axial direction.
μ	Coefficient of friction.
n	Hardening exponent.
N_i	Shape function.
$\{P\}$	Basic load vector.
$[Q]$, Q_{ij}	Transformation vector, component.
$\{R\}$	Unbalance force vector.
$\{\widehat{R}\}$	Condensed form of unbalance force vector.
$\boldsymbol{R}$, R_{ij}	Rotation tensor, component.
$[R]$	Matrix representation of components of $\boldsymbol{R}$.
$\boldsymbol{S}$, S_{ij}	Second Piola-Kirchoff stress tensor, component.
$[S]$	Matrix representation of components of $\boldsymbol{S}$.
S_f	Surface with traction applied.

tol_t	Tolerance for convergence of the numerical method.
$\{u_1\}$	Displacement vector corresponding to nodes of type 1.
$\{u_2\}$	Displacement vector corresponding to nodes of type 2.
$\{u\}$	Total displacement vector.
$\{\hat{u}\}$	Condensed form of displacement vector.
$\{\Delta u^I\}$	Displacement vector due to basic load vector.
$\{\Delta u^{II}\}$	Displacement vector due to unbalanced force vector.
U, U_{ij}	Right stretch tensor, component.
$[U]$	Matrix of Right stretch tensor.
$[U^p]$, U^p_{ij}	Matrix representation of the components of U with respect to principal axes, component.
V	Volume.
W, W_{ij}	Spin tensor, component.
x_i	Co-ordinate of generic particle.
δ	Variation.
δ_{ij}	Kronecker delta.
Δ	Increment in quantity.
ε, ε_{ij}	Small strain tensor, component.
$[\varepsilon]$	Matrix representation of ε.
ε^p_{eq}	Equivalent plastic strain.
$[\varepsilon^L]$, ε^L_{ij}	Matrix representation of the components of logarithmic strain tensor with respect to principal axes, component.
ε^{pL}, ε^{pL}_{ij}	Plastic part of $[\varepsilon^L]$, component.
η, η_{ij}	Non-linear part of the Green-Lagrange strain tensor, component.
λ_i	Principal stretch component.

λ, μ	Lame's constants.
ν	Poisson's ratio.
ρ	Density.
σ, σ_{ij}	Cauchy stress tensor, component.
$[\sigma]$	Matrix representation of σ.
$\dot{\sigma}, \dot{\sigma}_{ij}$	Cauchy stress rate tensor, component.
$\overset{o}{\sigma}, \overset{o}{\sigma}_{ij}$	Jaumann stress rate tensor, component.
σ_y	Yield stress.
σ_m	Hydrostatic stress.
$[\sigma^M], \sigma_{ij}^M$	Matrix representation of the components of the stress tensor with respect to a material frame, component.
σ', σ_{ij}'	Deviatoric part of the Cauchy stress tensor, component.
ϕ	Diameter of the workpiece.
$\{\Phi_i\}$	Array of shape functions.

Chapter 1

INTRODUCTION AND LITERATURE REVIEW

1.1   Introduction

Forging is a process in which the workpiece is shaped by compressive forces applied through various dies and tools. It is one of the oldest metalworking processes known to the mankind. It was first used to make jewelry, coins and various implements. Today, from a simple rivet to the landing gear of aircraft or from an automobile connecting rod to the propeller shaft for ship, forged products have quite a wide spectrum of applications. Good strength and toughness of the forged parts is the main reason for this. These properties can be achieved since grain orientation and grain size are controllable in forging process.

Forging may be performed at room temperature (cold forging) or at elevated temperatures (hot forging). Cold-forged parts have good surface finish and dimensional accuracy but because of higher strength of the material, cold forging requires greater forces, hence the workpiece materials must have sufficient ductility at room temperature. Less ductility, micro-structural faults in original metal, incorrect die design, improper heating and lubrication, large and rapid reduction, nonuniform deformation of material etc. can cause forging defects. Barreling, tears (surface cracks), edge cracks, central cavity, thermal cracks, laps, fins, wrinkles (orange peel), end grains etc. are the defects seen in forged parts [54]. Defects are undesirable because these reduce the strength of the forged parts which are intended to be used in critical stress applications. Several ductile fracture criteria are used to predict cracks in forging [65,69] and need exact stress and strain values to predict micro-crack formation. The finite element method can estimate stresses and strains to a good degree of accuracy. In the present work, an elasto-plastic FEM analysis of axisymmetric upsetting of cylindrical billet is carried out and damage distribution is predicted using a continuum damage mechanics model, proposed recently by Dhar [46,75].

1.2 Literature Review

1.2.1 Deformation Analysis of Forging Process

The problem of upsetting of metals has theoretical as well as technological significance in that its solution help in bringing about a better understanding of the behaviour of metals during plastic deformation at high pressure. Such solutions may also give specific answers to problems actually encountered in practice. It is for this reason that a number of investigators have dealt with the forging problem. Early investigators considered the material as an ideal-plastic solid i.e. rigid perfectly-plastic solid. This leads to so called slip line solution. Such solutions have been proposed by Prandtl, Hill et al. [1], and Green [2]. The slip line theory has been well developed to analyze a non-homogeneous plane strain deformation of an ideal-plastic solid. This theory can be used to get very good first approximations to loads required or to provide indications of the manner in which material deforms. However, the elastic effect can not be incorporated and work hardening is difficult to incorporate in this method and it is not suitable for axisymmetric problems. Further, residual stresses also cannot be studied using this technique. Shabaik [3] investigated the bulging in upsetting by using the slip line theory.

Hoffman and Sach [4] proposed the slab method. A complete analysis of the slab method has been presented by Altan [5] for the axisymmetric closed die forging. In this method, a slab of infinitesimal thickness is selected and then the force equilibrium equation for the slab is written, assuming that the deformation is homogeneous within the slab and the major directions are the principal stress directions. The resulting differential equation is then solved with appropriate boundary conditions. While this method can give very good predictions of the load variation with deformation, it is inherently incapable of predicting shape changes such as barrelling in open die forging. Further, since this method is primarily based on the assumption of homogeneous deformation, it possibly cannot predict the residual stresses as they are caused by non-uniform deformation.

The upper bound theorem was formulated by Prager and Hodge [6]. If surfaces of velocity discontinuities are included [7], then it states that among all kinematically admissible velocity fields v_i^*, the actual one minimizes the following expression

$$J^* = \int_V S_{ij}^* \varepsilon_{ij}^* dV + \int_{S_\Gamma} \tau \left| \Delta v^* \right| ds - \int_{S_t} T_i v_i^* ds \; , \qquad (1.1)$$

Here, $\dot{\epsilon}_{ij}^*$ is the strain rate field derived from v_i^*, S_{ij}^* is the deviatoric stress field derived from $\dot{\epsilon}_{ij}^*$ and $\left| \Delta v^* \right|$ is the discontinuity in the tangential component of the velocity across the surface S_Γ. Further, τ denotes the shear stress on the surface S_Γ and T_i is the prescribed traction on the part S_t of the boundary. The first term expresses the power spent in causing the internal deformation over the volume V of the deforming body. The second term represents

the power loss over the surfaces of velocity discontinuities including the boundary between tool and material. The last term represents the power supplied by specific tractions. What the upper bound theorem states is that the actual externally supplied power is never higher than that computed by the first two terms of the above equation.

Kudo [8] applied the upper bound theorem to the problem of plane strain forging and extrusion. Kudo [9] also applied this to the analyses of axisymmetric cold forging and extrusion. McDonald et al. [12], Kobayashi [11], Avitzur [10] and many others have suggested upper bound velocity fields to predict forging load in upsetting with bulging. Yang and Kim [13], Kim et al. [14] and Manuel et al. [15] have proposed upper bound method for analysis of three-dimensional upset forging. The major difficulty in using upper bound method is how to choose a kinematically admissible velocity field since the accuracy of the solution depends on how close the assumed velocity is to actual one. Another disadvantage of the method is that the solution provided by the method does not satisfy the equilibrium equations. So, even if elastic effects are included in integral (1.1), the method possibly cannot be used for the determination of residual stresses.

Accurate determination of forging parameters under realistic conditions became possible when the finite element method (FEM) was introduced. The major advantage of FEM is that it can be applied to a wide class of boundary value problems without restrictions on workpiece geometry. Using FEM, it is possible to predict the platen forces, the interface pressure and the stress, strain and residual stress distributions within the billet at various deformation levels.

Early applications of the FEM to forging problems were based on the incremental method proposed by Lee and Kobayashi [16]. The method uses the elastic-plastic strain matrix based on Prandtl-Reuss equations. The additivity of incremental elastic and plastic strains is assumed. Even though the stress-strain matrix and the geometry are updated after every increment, only the linearized incremental equations are used. The method was applied to solid cylinder upsetting [17], ring compression [18] and for predicting defects in upsetting [19]. Maccarini et al. [20] used the method for studying the influence of die geometry on cold extrusion forging operation. Where as Lee and Kobayashi [16] used the velocity as the primary unknown, Hartley et al. [21,22] proposed an incremental method with the displacement as the primary unknown. In Hartley's method, the linearized equations are used and the elasto-plastic matrix and the geometry are updated after every increment. Shima et al. [23] proposed a rigid-plastic finite element model based on plasticity theory for porous materials. They used Coulomb's law to model the friction at the workpiece-die interface. They applied this method to upsetting of a cylinder and validated their results by conducting experiments. Three-dimensional elasto-plastic finite element analysis has been done by Pillinger et al. [24] using linearized incremental equations.

Linearized incremental equations give only an approximate solution. If the incremental

size is not sufficiently small, the error between the exact and the approximate solutions grows rapidly with the applied load, as the error in the solution of the current increment gets propagated into the next increment when the stress-strain matrix and the geometry are updated. To avoid this phenomenon, non-linear incremental equations should be solved by using a scheme like Newton-Raphson technique. Such a formulation was first proposed by Bathe et al. [25]. this formulation (with or without elastic effects) has been applied to the forging problem by quite a few researchers. It was applied by Dadras and Thomas [26] and Carter and Lee [27] to axisymmetric upsetting. Dadras and Thomas have also developed the kinematically admissible velocity fields for different deformation zones by means of empirical equations.

Some of the typical references in this area are as follows. Most of them use iterative method to solve the non-linear incremental equations. Michel and Boyer [28] carried out the elasto-visco-plastic finite element analysis of cold upsetting process and did its experimental validation. However, they used the friction factor model. Therefore, their results could not be used to validate the proposed finite element model, which uses the Coulomb friction model. Lin [29] has proposed a new model for inter-facial friction in which the friction coefficient changes continuously with the reduction in height. The experimental measurements on the barrelling of the free surface are used to determine the functional dependence of the friction coefficient on the reduction in height. Further, he assumed the flow stress to depend on strain, strain rate and temperature. Even though his model is in good agreement with experiments on cold upsetting, it is a little too sophisticated to be of use to practical problems. Yang et al. [30] have proposed a 3-D finite element model in which the workpiece and die are analyzed together. The workpiece-die contact is classified into three cases: (I) No contact, (II) sliding contact and (III) cohesive contact. Multi-substructure technique is used to reduce the size of the problem. Their model incorporates the determination of temperature field as well as the residual stress distribution. However, no results on residual stresses are reported. Joun et al. [31] have proposed a computer simulation technique for forging process which uses a spring attached-die. The strategy of spring attached-die control the metal flow lines in such a fashion that it results in prevention of defects and improvement of product quality.

The thrust of most of the above studies has been either to find an accurate estimation of forging load or to study deformation field. A major difficulty observed in all the previous attempts is that the increment size has to be very small in order to achieve a reasonable level of accuracy in the stress values. This leads to prohibitively large amount o computational time. The Jaumann stress measure, which is the objective stress measure used presently in the literature, does not give accurate stress values if the incremental shear deformation is large. Thus, there is a need to look for a new objective stress measure, which will allow the use of a large incremental size without compromising the accuracy of stresses. Such a measure has been recently proposed in reference [33].

1.2.2 Ductile Fracture Criteria

Ductile fracture is often a limiting factor in many metal forming processes. It is well known that ductile fracture occurs due to micro-void nucleation, growth and finally coalescence into micro crack. Many ductile fracture criteria have been proposed and applied to predict ductile fracture in plastically deforming metals including metal forming processes. This section reviews some of the published ductile fracture criteria.

The published ductile fracture criteria can be broadly classified into two groups. They are

- Models based on microscopic observations about void nucleation, growth and coalescence

- Empirical and semi-empirical models

Three broad approaches have emerged which try to predict ductile fracture (micro-crack initiation) on the basis of void nucleation, growth and coalescence. They are

- Models of porous plasticity

- Models of void nucleation, growth and coalescence

- Continuum damage mechanics models

Models of Porous Plasticity

In these models, the material with voids is idealized as porous material. Thus, its constitutive equation is derived from the plastic potential of porous materials. In a porous plastic material, there is a possibility of dilatation because of which the yield surface does not remain an infinitely long cylinder like that of an incompressible material but is capped by elliptical surfaces.

Gurson's Model

Gurson [34] proposed a plastic potential function for a porous solid with randomly distributed voids of volume fraction V_f in the form

$$\Phi = \frac{\bar{\sigma}_p^2}{\bar{\sigma}^2} + 2V_f cosh(\frac{3\sigma_{m_p}}{2\bar{\sigma}}) - (1 + V_f^2) = 0 \tag{1.2}$$

where $\bar{\sigma}_p$ and σ_{m_p} are the generalized and hydrostatic stresses of the porous aggregate and $\bar{\sigma}$ is the generalized stress of the void free (incompressible) matrix.

In this model, the growth rate of void volume fraction is considered partly due to the growth of the existing voids and partly due to the nucleation of new voids. i.e.,

$$\dot{V}_f = \dot{V}_{f-growth} + \dot{V}_{f-nucleation} \tag{1.3}$$

The rate of change of the void volume fraction due to the growth of existing voids is related to the mean strain rate $\dot{\epsilon}_n$ by the relation

$$\dot{V}_{f-growth} = (1 - V_f)\dot{\epsilon}_n \tag{1.4}$$

In general, void nucleation rate depends on both the generalized strain rate as well as the rate of increase of hydrostatic stress. In this model, void nucleation rate is assumed to depend only on the generalized strain rate by the relation

$$\dot{V}_{f-nucleation} = A\dot{\bar{\epsilon}} \tag{1.5}$$

where A is a constant.

Gurson's criterion [34] was modified by Tvergaard [35] and Needleman and Tvergaard [36] by introducing some constant (q_1) to bring the predictions of the model into closer agreement with numerical analysis of a periodic array of voids. The modified criterion is given by

$$\Phi = \frac{\bar{\sigma}_p^2}{\bar{\sigma}^2} + 2V_f q_1 cosh(\frac{3\sigma_{m_p}}{2\bar{\sigma}}) - (1 + (q_1 V_f)^2) = 0 \tag{1.6}$$

where q_1 is a constant.

In this model, ductile fracture is regarded as the result of an instability in the dilatational plastic flow field localized in a band (called the shear band). The fracture criterion is represented as a graph of critical localization strain versus the critical void volume fraction with strain hardening exponent as a parameter.

Oyane's Model

Oyane [37] and Oyane et al. [38] used the plasticity theory for porous materials to propose a ductile fracture criterion indicating that micro crack initiates whenever the volumetric strain reaches a material dependent critical value. For pore free materials, assuming that the material obeys porous plasticity equations after the initiation of voids, Oyane obtained the criterion for ductile fracture as

$$\int_0^{\epsilon_{vf}} f_\rho^2 \rho_r^{2n-1} d\epsilon_v = C \tag{1.7}$$

where f_ρ is a function of relative density ρ_r which is defined as the ratio of the apparent density of the porous material to the density of the pore free matrix, ϵ_{vf} is the volumetric strain at fracture and n and C are constants. The constant C is given by

$$\int_{\bar{\epsilon}_i}^{\bar{\epsilon}_f} (1 + \frac{\sigma_m}{A\bar{\sigma}})d\bar{\epsilon} = C \tag{1.8}$$

where $\bar{\epsilon}_i$ is the generalized strain at which voids get initiated, $\bar{\epsilon}_f$ is the generalized strain at which fracture occurs and A is a material constant. By assuming that $\bar{\epsilon}_i = 0$, the above criterion reduces to a simple form

$$\int_0^{\bar{\epsilon}_f} (1 + \frac{\sigma_m}{A\bar{\sigma}})d\bar{\epsilon} = C \tag{1.9}$$

For porous materials, they modified the criterion by including the relative density term into the integral. Thus,

$$\int_0^{\bar{\varepsilon}_f} (1 + \frac{\sigma_m}{A\rho_r^n\bar{\sigma}})d\bar{\varepsilon} = C\rho_0^B \tag{1.10}$$

Here $\rho_r^n\bar{\sigma}$ is the generalized flow stress of the porous material, B is a constant and ρ_0 is the initial relative density of the porous material. A method for estimating values of the material constants using the compression test has been provided by them.

The major limitation of the above two criterion is that they do not model ductile fracture (i.e. micro-crack initiation) as a void coalescence phenomenon.

Models of Void Nucleation, Growth and Coalescence

The void nucleation model of Goods and Brown [39], the void growth models of McClintock [40] and Rice and Tracey [41] and void coalescence model of Thomason [74] along with some additional models on void nucleation and growth are discussed in this section.

Models of Void Nucleation

Goods and Brown [39] developed a stress based void nucleation model based on the condition that the voids nucleate by decohesion of particles whenever the normal stress reaches a critical value (σ_c) at the particle/matrix interface. They obtained a relation between the void nucleation strain (ϵ_1^n) and hydrostatic stress (σ_m) as

$$\epsilon_1^n = Kr_p(\sigma_c - \sigma_m)^2 \tag{1.11}$$

where K is a material constant dependent on the particle volume fraction and r_p is the particle radius. Experiments on Fe-Fe$_3$C system [39] confirm the linear relationship between the nucleation strain and particle radius. This relation is for small spheroidal particles of radius less than or equal to $1\mu m$.

For large size particles, the approximate analysis of Argon and Im [42] gives the condition for the void nucleation by decohesion as

$$\bar{\sigma} + \sigma_m = \sigma_c \tag{1.12}$$

For a given problem, this condition can be expressed in terms of the nucleation strain. Note that this relation is independent of particle radius.

Gurland [43] proposed a nucleation model based on the experiments conducted by him on 1.05% C spheroidal steel. Experimental observations reveal that the void nucleation occur by cracking of cementite particles. Voids nucleate at all strain levels depending on the size, shape and orientation with the maximum principal stress direction. It is observed that the volume fraction of broken particles is a linear function of the plastic strain.

Void Growth Models

Once the nucleation of micro-voids takes place either by decohesion or cracking of a secondary particle or inclusion, the resulting stress free surface of the void produces a localized stress and strain concentration in the plastically surrounding matrix. With continuing plastic flow of the matrix, the void undergoes volumetric growth and change of shape. Some of the published void growth models are discussed here.

McClintock [40] proposed a void growth model for two-dimensional plane strain problems considering a single elliptic void. He assumed that the major and minor axes of the void coincide with the principal stress directions. He obtained the following closed form expression for void growth in a rigid work-hardening material whose generalized stress relation is $\bar{\sigma} = K \bar{\epsilon}^n$:

$$ln \frac{R_h}{R_{0h}} = \frac{\sqrt{3}\bar{\epsilon}}{2(1-n)} \sinh \frac{\sqrt{3}(1-n)}{2} \frac{\sigma_a + \sigma_b}{\bar{\sigma}} + \frac{\epsilon_a + \epsilon_b}{2} \tag{1.13}$$

where R_h and R_{0h} are the current and initial mean radii of the hole respectively, σ_a and σ_b are the principal stress and ϵ_a and ϵ_b are the principal strain components along the major and minor axes respectively. Fracture was assumed to occur at the point where a growing void touches the cell boundary. Dung [44,45] modified and extended McClintock's model [40] to analyze the growth of circular/elliptic voids in plane strain problems and spherical/ellipsoidal voids in three-dimensional problems.

Rice and Tracey [41] considered a single spherical void of initial radius R_{0v} in a remote uniform strain rate field $\dot{\epsilon}_{ij}$ and remote stress field σ_{ij} in a rigid plastic material. They obtained the following expression for the rate of change of the radii ($\dot{R}_{kv}$) of the void in the principal strain rate directions:

$$\dot{R}_{kv} = \{(1+F)\dot{\epsilon}_k + \dot{\bar{\epsilon}}H\}R_{mean} \tag{1.14}$$

where
$$F = \tfrac{2}{3} \text{ for linear hardening and for low values of } \sigma_m \text{ for non hardening}$$
$$= 1 \text{ for high values of } \sigma_m \text{ for non hardening}$$
$$H = 0.75\tfrac{\sigma_m}{\bar{\sigma}} \text{ for linear hardening}$$
$$= 0.558 \sinh \tfrac{3}{2}\tfrac{\sigma_m}{\bar{\sigma}} + 0.008\nu \cosh \tfrac{3}{2}\tfrac{\sigma_m}{\bar{\sigma}} \text{ for non hardening,}$$

$$R_{mean} = \tfrac{1}{3}(R_{1v} + R_{2v} + R_{3v})$$

$$\dot{\bar{\epsilon}} = \text{generalized strain rate}$$

$$\dot{\epsilon}_k = \text{principal strain rates}$$

$$\nu = -\tfrac{3\dot{\epsilon}_2}{\dot{\epsilon}_1 - \dot{\epsilon}_3}, \text{ Lode variable.}$$

Note that an initial spherical void grows into an ellipsoidal void of principal radii R_{1v}, R_{2v} and R_{3v}. Thomason [74] integrated the above equation by assuming that the principal axes of

strain rates remain fixed in direction throughout the strain path and obtained the following expressions for the principal radii of the void:

$$R_{1v} = \left(A + \frac{3B(1 + \nu)}{2\sqrt{\nu^2 + 3}} \right) R_{0v} \tag{1.15}$$

$$R_{2v} = \left(A - \frac{\nu B}{\sqrt{\nu^2 + 3}} \right) R_{0v} \tag{1.16}$$

$$R_{3v} = \left(A + \frac{(\nu - 3)B}{2\sqrt{\nu^2 + 3}} \right) R_{0v} \tag{1.17}$$

where

$$A = \exp \frac{2\sqrt{\nu^2 + 3}}{3 + \nu} H \epsilon_1^g$$

$$B = \frac{1 + F}{H}(A - 1)$$

and ϵ_1^g is the integral of the largest principal strain rate. Thomason [74] used the above expressions in the derivation of the void coalescence condition.

For an array of void nucleating particles of diameter D_p and spacing d_s, setting the initial void radius as $D_p/2$, eqns. (1.12) and (1.13) leads to the following expression for fracture strain:

$$\bar{\epsilon}_f = \frac{\ln(d_s/D_p)(1 - n)}{\sinh[(1 - n)(\sigma_a + \sigma_b)/(2\bar{\sigma}/\sqrt{3})]} \qquad [\text{McClintock}, 1968] \tag{1.18}$$

$$\bar{\epsilon}_f = \frac{\ln(d_s/D_p)}{0.28 \ \exp(1.5\sigma_{kk}/\bar{\sigma})} \qquad [\text{Rice and Tracey}, 1969] \tag{1.19}$$

Some research workers have used the above expressions for the prediction of ductile fracture with the help of experimentally determined parameters. The major limitations of this approach are that it ignores the effects of void nucleation (as the expressions are derived from a pre-existing finite size void) and void coalescence. Thus, $\bar{\epsilon}_f$ is usually overestimated.

Void Coalescence Model

Thomason [74] modeled void coalescence phenomenon as plastic instability due to necking of the inter void matrix. The sufficient condition for plastic instability of the inter-void matrix, as given by him, is

$$\sigma_n \bar{A}_n - \sigma_1 = 0 \tag{1.20}$$

where $\bar{A}_n$ is the area fraction of the inter-void matrix perpendicular to the direction of maximum principal stress σ_1 and σ_n is the plastic constraint stress. He considered a geometrically equivalent square prismatic void and used the upper bound method to obtain an expression for the plastic constraint stress in terms of the void dimensions, inter-void spacing and the yield stress.

Thomason [74] combined the results of Goods and Brown [39] on void nucleation, Rice and Tracey [41] on void growth and his own on void coalescence to arrive at a fracture criterion. He used expressions (1.14 to 1.16) for the void dimensions to express the void coalescence condition (eqn. 1.19) in terms of the void growth strain ϵ_1^g and the hydrostatic stress σ_m. By superposing this condition on the void nucleation relation (eqn. 1.10), he obtained the fracture criterion as a graph of fracture strain ($\bar{\epsilon}_f = \epsilon_1^n + \epsilon_1^g$) versus the triaxiality (i.e. the ratio of hydrostatic stress to the generalized stress).

The main drawback of this approach is the use of expressions (1.14 to 1.16) for void growth. These expressions are based on integration procedure which assumes that the principal directions of strain rate remain fixed throughout the strain path. This is, in general, true only for the case of small strain and rotation. As a result, this approach cannot be used when the strains and/or rotations are large.

Continuum Damage Mechanics Models

In these models, material behavior is represented by a plastic potential which includes damage as an internal variable. The damage variable quantifies the intensity of voids, which can be identified as either the void volume fraction or the area void fraction. The basis of continuum damage mechanics models rests on the theory of continuum thermodynamics. In this section some of the continuum damage mechanics models are discussed.

Lemaitre [47] proposed a continuum damage mechanics model for void growth in elasto-plastic materials with area void fraction as the damage variable using the concepts of effective stress and strain equivalence. His model is based on a simple damage growth law in which the damage rate is linearly dependent on the plastic strain and the thermodynamic force corresponding to the damage. It does not account for void nucleation. Note that, as far as void coalescence is concerned, it has to be incorporated as an additional condition in terms of the continuum parameters. This condition, which serves as a fracture criterion, has to be based on an appropriate micro model. Thomason's limit load model seems to be a good candidate for this purpose.

More recently Dhar [46] and Dhar et al. [75] extended Lemaitre's [47] continuum damage mechanics model to incorporate a damage growth law which accounts for both the void nucleation as well as void growth. The law is based on the experimental results of Le roy et al. [48]. They also modified Thomason's [74] void coalescence condition to make it suitable for the case of large strain and/or rotation. They combined the extended continuum damage mechanics model and modified void coalescence condition to arrive at a criterion for prediction of micro crack initiation. The salient features of the above approach are discussed below.

In this model, damage D is identified as an area void fraction at a point in a plane. Thus,

it is defined by

$$D = \frac{\Delta A_v}{\Delta A} \qquad (1.21)$$

where ΔA is the infinitesimal area around the point in some plane and ΔA_v is the area of the voids in the plane containing ΔA. The conjugate variable corresponding to D is $-Y$, the rate at which the elastic energy releases during the damage growth at constant stress. For an isotropic material, $-Y$ is given by [47]

$$-Y = \frac{\bar{\sigma}^2}{2E(1-D)^2} f(\frac{\sigma_m}{\bar{\sigma}}) \qquad (1.22)$$

where

$$f(\frac{\sigma_m}{\bar{\sigma}}) = \frac{2(1+\nu)}{3} + 3(1-2\nu)(\frac{\sigma_m}{\bar{\sigma}})^2 \qquad (1.23)$$

Here, E is the Young's modulus, ν is the Poisson's ratio and $(\sigma_m/\bar{\sigma})$ is called the triaxiality. The damage growth law is given by

$$\dot{D} = C_D \dot{\bar{\epsilon}} + (a_1 + a_2 D)(-Y)\dot{\bar{\epsilon}} \qquad (1.24)$$

where a_1, a_2 and C_D are material constants. Here the first term, which is independent of $-Y$, represents the damage evolution due to void nucleation while the second term, which is dependent on $-Y$, represent the evolution of damage due to void growth. For SAE 1090 steel, Dhar et al. [75] determined the constants fitting eqn. (1.23) through the experimental results of Le Roy et al. [48]. They obtained the following values:

$$C_D = 1.898 \times 10^{-2}$$
$$a_1 = 9.8 \times 10^{-4} \text{ MPa}^{-1}$$
$$a_2 = 1.84 \text{ MPa}^{-1}$$

While getting these constants, they used Bridgman's relation [49] to express the triaxiality as a function of strain.

Dhar et al. [75] used finite strain expressions for the void dimensions and inter-void spacing to express Thomason's void coalescence criterion (eqn. 1.19) in the following form:

$$\sigma_1 \left[0.1 + \frac{1.2}{\{1 - \exp(-\bar{\epsilon}/2)\}^{0.5}} \right] \exp(-\bar{\epsilon})\,\bar{\sigma} = 0 \qquad (1.25)$$

where $\bar{\epsilon}$, the generalized strain, is the integral of $\dot{\bar{\epsilon}}$ along the path lines. To find the critical value of damage parameter (D_c), they applied this criterion to various geometries and loading conditions using the elasto-plastic finite element analysis. They observed that D_c is independent of geometry or loading and hence that can be used as a material property for the prediction of micro-crack initiation. They reported that the value of D_c is 0.05 for SAE 1090 steel.

Empirical and Semi-Empirical Models

In the absence of reliable quantitative models for incorporating the phenomena of void nucleation, growth and coalescence in materials undergoing large plastic deformation in metal forming processes, many empirical relations based on some phenomenological models have been proposed. This section reviews some of them.

Freudenthal [50] postulated that generalized plastic work per unit volume is the critical parameter and is expressed as

$$\int_0^{\bar{\varepsilon}_f} \bar{\sigma} d\bar{\varepsilon} = C_1 \tag{1.26}$$

Cockcroft and Latham [51] modified the generalized plastic work criterion to take care of the effects of change in the neck geometry which is observed in tensile tests. The criterion is given by

$$\int_0^{\bar{\varepsilon}_f} \bar{\sigma} \frac{\sigma_1}{\bar{\sigma}} d\bar{\varepsilon} = \int_0^{\bar{\varepsilon}_f} \sigma_1 d\bar{\varepsilon} = C_2 \tag{1.27}$$

Here σ_1 is the maximum normal stress.

Oh et al. [19] modified Cockcroft and Latham criterion [51] by considering the ratio of the maximum tensile stress to the generalized stress. This criterion is expressed as

$$\int_0^{\bar{\varepsilon}_f} \frac{\sigma_1}{\bar{\sigma}} d\bar{\varepsilon} = C_3 \tag{1.28}$$

The main drawback of the above three criteria is that the effect of hydrostatic stress is not considered. Osakada and Mori [52] developed a ductile fracture criterion which includes the effects of both plastic strain and hydrostatic stress and expressed it as

$$\int_0^{\bar{\varepsilon}_f} < a + \bar{\varepsilon} + b\sigma_m > d\bar{\varepsilon} = C_4 \tag{1.29}$$

$$< \bullet > = \bullet \qquad \bullet \geq 0$$

$$< \bullet > = 0 \qquad \bullet < 0$$

where a and b are material constants.

Norris et al. [53] developed a fracture criterion based on their experimental results and finite difference results of several test geometries and expressed it as

$$\int_0^{\bar{\varepsilon}_f} \frac{1}{(1 - C\sigma_m)} d\bar{\varepsilon} = C_5 \tag{1.30}$$

where C is a constant.

In the above equations $C_1, \cdots C_5$ are the critical values accumulated over the strain path to fracture.

1.2.3 Defects in Forging

Different type of defects are observed in industrial metal forming processes which are tabulated by Johnson and his co-workers [59, 64, 66]. The limit of forming processes is governed by the material properties, friction, temperature, rate of deformation and geometry. It is a well established fact that the tensile triaxiality is the main factor contributing to the crack initiation in these processes.

There are several defects found in open die forging namely barreling, tears or surface cracks, centre burst, thermal cracks, end grains etc. Barreling occurs due to friction between the part and the die or when there is a large temperature difference between the part and the die. This leads to greater deformation in the midsection of the part than in the constrained ends [58]. The amount of barreling is more for unlubricated conditions [56]. Thermal cracks are the result of non-uniform temperatures within a metal. When flow lines reach a surface perpendicularly, exposing the grain boundaries directly to the environment, this condition is known as end grains.

Cracks due to tangential velocity discontinuities or edge cracks (i.e. at the work-die interface) may arise in the material which is insufficiently ductile or when friction at the interface is high. In simple upsetting, longitudinal cracking occurs at the barreled surface due to presence of secondary tensions. A central cavity is a rupture occurring at the centre of the billet [54].

Thomason's [55] uniaxial compression test results support the hypothesis that a metal must reach a state of tensile plastic instability before ductile fracture. He observed ductile fracture occurred on the surface of uniaxial compression specimens without any evidence of external local necking.

Kobayashi [56] conducted a number of experiments with different height-diameter ratios in varying friction conditions. He reported that normal fracture occurred when friction was severe and the axial stress was tensile and when friction was less severe, the axial stress at fracture was compression and the fracture was of a shear type.

Kuhn and Lee [57] conducted experiments on steel cylinders under varying conditions. A refined measurements of strains revealed that the axial strain suddenly reached a plateau and remained constraint while the hoop strain continued to increase. The axial strain then resumed its increase and did so at the same rate as the hoop strain. They interpreted this strain perturbation as a localized instability in strain and hence localized necking of material, between inhomogeneities, which eventually led to fracture. Also they metallographically detected void formations prior to fracture.

Sowerby, Dung et al. [60,62] examined the capability of McClintock's void growth model to predict damage accumulation in the upsetting of steel specimens using rigid-plastic formulation and found it appropriate for homogeneous metals. Predeleanu et al. [63] conducted

experiments and computer simulations using their damage criterion and found that material damage reaches a critical value inside the specimen and not at the free surface. They also detected voids and micro-cracks within the interior of the specimen before surface fracture.

Clift et al. [61,65] used 3-D elasto-plastic finite element analysis using 8-noded brick element. They modeled boundary friction conditions by defining an extra layer of elements, referred to as the friction layer on the required surfaces. But they didn't report effect of friction in their study. The numerical results were used to give predictions of fracture initiation site for a total of nine fracture criterion. They compared these predicted sites with experiments and showed that generalized plastic work per unit volume criterion is capable of estimating the experimental fracture initiation sites for the complete range of processes considered. They re-confirmed that the fracture criterion proposed by Ghosh was not successful in any one of the cases examined. Later Zhu et al. [67,69] also disapproved Ghosh criterion in their simulation on side pressing of cylindrical billets. The main reason for the failure of Ghosh's criterion is that it was proposed for sheet metal forming, not for bulk metal forming.

Lin and Lin [68] used strain energy density failure criterion in conjunction with coupled thermo-elasto-plastic large deformation model to analyze ductile fracture in upsetting of the cylindrical specimen under various geometrical and frictional conditions. They reported increased damage with higher friction.

Semiatin et al. [72] conducted hot forging trials on Ti-6Al-4V specimens and validated the results with finite element analysis and suggested that the Rice and Tracey void growth model which highlights that the influence of hydrostatic stress and Cockroft and Latham criterion provided good estimate of surface fracture.

Atkins [70] found that well lubricated cylinders developed inclined cracks found in shear while unlubricated ones showed vertical cracks formed in tension. He also mentioned that the greatest strains to fracture occur at the least values of tensile hydrostatic stress.

Recently, Kim, Im and Geiger [73] investigated the ductile fracture criterion based on work hypothesis and Cockcroft and Latham criterion, and carried out experiments and rigid-visco-plastic finite element analysis studies on simple upsetting of aluminium billets. They deduced that Cockcroft and Latham's criterion gave a more reasonable prediction for crack initiation site than work hypothesis and the former was useful in processes like cold forging in which the influence of the induced circumferential tensile stress on failure is dominant.

Gouveia et al. [71] used finite element analysis and experimental results to analyze four ductile fracture criteria in forging. They reported that Freundenthal criterion predicted much higher values of damage inside the specimen and thus located fracture initiation site at the center of the billet. The drawback of Cockroft-Latham criterion, they suggested, was if the largest principal stress σ_1 is temporarily negative led to accumulation of negative damage. They concluded that the Oyane's criterion which is formulated on the basis of the void growth model and the theory of the plasticity of the porous media, was the best among the criteria

considered.

The above studies show that published ductile fracture criteria have had only limited success in predicting the fracture in forging process. Further, different experimental set-ups seem to give different values of the critical material parameters required in the criterion. A universal criterion which can be applied to all forging problems has yet to come up.

1.3 Scope and Objective of the Present Work

In the present work, damage in axisymmetric cold forging process is studied. An axisymmetric large deformation elasto-plastic finite element code is developed. The Updated Lagrangian formulation, which is convenient for handling material and geometric non-linearities, is used. New incremental objective stress measure and logarithmic strain measure are used instead of Jaumann stress rate and Green-Lagrange nonlinear strain tensors used in most of the literature. Forging problem is a displacement-controlled problem. Therefore, to accelerate the convergence of iterative scheme, arc length method is used in conjunction with modified Newton-Raphson iteration technique. The material is assumed to be elasto-plastic strain hardening and yielding according to von Mises criterion. Inertial forces and body forces are not included in the present work. Coulomb's law is used to model friction at the die-workpiece interface.

Review of the published research reveals that there have been several attempts to predict the occurrence of cracks in forging. But most of the fracture criteria used are empirical ones and they have had only a limited success. Ductile fracture in metal forming processes is now established as a void nucleation, growth and coalescence phenomenon. Dhar et al. [75] combined the continuum damage mechanics model of Lemaitre [47] with the void coalescence criterion of Thomason [74] to propose a criterion for micro-crack initiation in terms of the critical value of the damage parameter. This criterion incorporates all the features of microscopic description of ductile fracture, namely void nucleation, growth and coalescence. In the present study, this criterion is taken to predict damage distribution in AISI-1090 steel workpiece. This material is chosen because of availability of the values of constants used in the criterion.

The code is checked for mesh and step size convergence. Next, a detailed parametric study of damage distribution is carried out to show the effect of coefficient of friction at the die-workpiece interface and the height to diameter ratio of blank. For typical values of coefficient of friction and the height to diameter ratio, axial, circumferential and hydrostatic stress distributions are studied.

1.4   Organization of the Thesis

The thesis is organized as follows. In the second chapter, the mathematical modelling of forging process, the axisymmetric finite element formulation and the boundary conditions are presented. The damage formulation is then discussed. Numerical scheme is presented at the end of chapter. In the third chapter, results for a typical case are presented. It also includes discussion on the parametric studies.

Chapter 2

Mathematical Modeling and Finite Element Formulation of Axisymmetric Forging Process

In this chapter, mathematical model and finite element formulation of a cold forging process are developed. The process is modelled as an axisymmetric problem. The description of motion, stress measures, strain measures and constitutive laws used in the formulation of the governing equations for static large deformation elasto-plastic problems are presented in sections 2.1-2.7. The finite element formulation is discussed in section 2.8. The boundary conditions for axisymmetric forging process are discussed in section 2.9. The damage formulation is outlined in section 2.10 and the solution procedure for solving the finite element equations is presented in section 2.11.

2.1 Updated Lagrangian Formulation

In the study of the deformation of a body subjected to external loading, often the original undeformed and unstressed state of the body is used for the formulation of its equation of motion. This is known as Lagrangian formulation. This formulation is convenient for small deformation, which is the case in majority of engineering problems. In such cases, the deformed configuration does not deviate much from the original one and hence the deformation can be described by an infinitesimal strain tensor, also known as the engineering strain tensor, for which the strain-displacement relations are linear. On the other hand, for large deformation problems, one has to use a finite strain measure, which is expressed by a nonlinear strain-displacement relation. Furthermore, the equations of motion when expressed in the reference configuration depend on the deformation. Hence, for large deformation problems, the Lagrangian formulation proves to be cumbersome with the governing equations being difficult to solve. In such cases, one solves the problem using an incremental method known as Updated Lagrangian formulation. In this formulation, it is assumed that the states of

stress and deformation of the body are known till the current configuration, say at time t. The main objective is then to determine the incremental deformation and stresses during an infinitesimal time step, Δt, i.e from time t to $t+\Delta t$. Here, the current configuration is used as the reference configuration for obtaining the incremental values. Unlike in the Lagrangian formulation, an incremental strain tensor is used. This methodology is particularly useful for elasto-plastic materials because the stress-strain relationship in such materials is usually expressed in an incremental fashion.

2.2 Kinematics of Finite Deformation

The relative deformation gradient tensor at time $t + \Delta t$ is defined by

$$^{t+\Delta t}_{t}F_{ij} = \frac{\partial \left(^{t+\Delta t}x_i\right)}{\partial^t x_j} = ^{t+\Delta t}_{t} x_{i,j} \; , \tag{2.1}$$

where $^t x$ and $^{t+\Delta t}x$ denote the position vectors of the particle at times t and $t + \Delta t$ respectively. When $^{t+\Delta t}_{t}F$ is not singular, the polar decomposition theorem [76] allows a decomposition of the form

$$^{t+\Delta t}_{t}F_{ij} = ^{t+\Delta t}_{t} R_{ik} \, ^{t+\Delta t}_{t}U_{kj} \; , \tag{2.2}$$

where $^{t+\Delta t}_{t}R$ is an orthogonal tensor representing the material rotation and $^{t+\Delta t}_{t}U$ is a positive definite symmetric tensor called right stretch tensor. The right stretch tensor can be diagonalized by the following transformation to obtain the principal stretches $^{t+\Delta t}_{t}\lambda_i$:

$$^{t+\Delta t}_{t}U^p_{ij} = ^{t+\Delta t}_{t} Q_{ik} \, ^{t+\Delta t}_{t}Q_{jl} \, ^{t+\Delta t}_{t}U_{kl} \; , \tag{2.3}$$

where $^{t+\Delta t}_{t}[Q]$ is orthogonal and

$$^{t+\Delta t}_{t}\lambda_i = ^{t+\Delta t}_{t} U^p_{ii} \; . \quad \text{(No Sum)} \tag{2.4}$$

The tensor $^{t+\Delta t}_{t}R$ and the transformation matrix $^{t+\Delta t}_{t}[Q]$ are used in the development of a stress measure while the incremental logarithmic strain definition is obtained from the $^{t+\Delta t}_{t}\lambda_i$.

2.3 Stress Measures

It is essential that an objective stress measure be used in the incremental theory of constitutive modeling to account for the rigid body rotation that may accompany deformation. The Cauchy stress tensor, which has great physical significance, is not objective and hence cannot be used directly in a constitutive equation. There are numerous objective stress measures, each with particular advantages and disadvantages. Some of them are discussed below.

One of the most commonly used objective stress tensor is the second Piola-Kirchoff stress tensor ${}^{t+\Delta t}_{t}S$ which can be related to the Cauchy stress tensor ${}^{t+\Delta t}\sigma$ using the concept of equivalent work between two configurations [78].

$$
{}^{t+\Delta t}_{t}S_{ij} = \frac{{}^{t}\rho}{{}^{t+\Delta t}\rho} \, {}^{t}_{t+\Delta t}x_{i,m} \, {}^{t+\Delta t}\sigma_{mn} \, {}^{t}_{t+\Delta t}x_{j,n} \,, \tag{2.5}
$$

where ${}^{t}\rho$ and ${}^{t+\Delta t}\rho$ are the densities at time t and $t+\Delta t$ respectively and ${}^{t}_{t+\Delta t}x_{i,m}$ denotes the derivative of ${}^{t}x_{i}$ with respect to ${}^{t+\Delta t}x_{m}$. The second Piola-Kirchoff stress tensor is energy conjugate with the Green-Lagrange strain tensor. This energy conjugate pair is used in the equation for predicting displacements in a predictor corrector solution procedure (see section 2.7).

Another commonly used objective stress rate measure is the Jaumann stress rate $\overset{o}{\sigma}$. It is related to the Cauchy rate $\dot{\sigma}$ by

$$
{}^{t}\overset{o}{\sigma}_{ij} \, \Delta t = {}^{t}\dot{\sigma}_{ij} \, \Delta t - {}^{t}\sigma_{ik} \, ({}^{t}W_{jk}\Delta t) - {}^{t}\sigma_{jk} \, ({}^{t}W_{ik}\Delta t) \,, \tag{2.6}
$$

where

$$
{}^{t}W_{ij}\Delta t = \frac{1}{2}({}_{t}\Delta u_{i,j} - {}_{t}\Delta u_{j,i}) \,, \tag{2.7}
$$

represents the component of the incremental spin tensor. Here, ${}_{t}\Delta u_{i,j}$ denotes the derivative of the incremental displacement vector ${}_{t}\Delta u$ with respect to ${}^{t}x$.

As pointed out by Metzger and Dubey [79], it is important that the stress measure used be compatible with the constitutive equation in addition to being objective. An incremental objective stress measure (as against objective stress rate measures) to be used in the generalized Hooke's law and in the elasto-plastic constitutive equation is developed below.

Two Cartesian reference frames (see Fig.2.1) are used.

1. The fixed frame.

2. A material frame which rotates and translates along with the material particle.

The material frame is defined so as to coincide with the principal axes of the right stretch tensor at time t so that the initially orthogonal axes do not get skewed at time $t + \Delta t$.
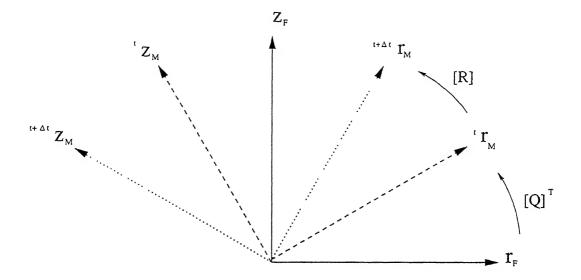
The first step in the derivation is the transformation of the components of the Cauchy stress tensor at time t from the fixed frame to the material frame:

$$
{}^{t}\sigma_{ij}^{M} = {}^{t+\Delta t}_{t}Q_{ik} \, {}^{t+\Delta t}_{t}Q_{jl} \, {}^{t}\sigma_{kl} \tag{2.8}
$$

The increment in the components of the Cauchy stress tensor with respect to the material axes, ${}_{t}\Delta\sigma_{ij}^{M}$, is added to ${}^{t}\sigma_{ij}^{M}$ to obtain the stress components at time $t + \Delta t$ with respect to the material frame of reference:

$$
{}^{t+\Delta t}\sigma_{ij}^{M} = {}^{t}\sigma_{ij}^{M} + {}_{t}\Delta\sigma_{ij}^{M} \tag{2.9}
$$

The fixed frame is denoted by subscript F,
the material frame is denoted by subscript M.

Figure 2.1: Fixed and material reference frames

The final transformation from the frame at time $t + \Delta t$ to the fixed frame give the components of the Cauchy stress tensor at time $t + \Delta t$:

$$^{t+\Delta t}\sigma_{ij} = {}^{t+\Delta t}_{t}Q_{ki} {}^{t+\Delta t}_{t}R_{kl} {}^{t+\Delta t}_{t}\sigma^{M}_{lm} {}^{t+\Delta t}_{t}R_{nm} {}^{t+\Delta t}_{t}Q_{nj} \tag{2.10}$$

The equations (2.8), (2.9) and (2.10) can be combined together to give a relation between the components of the Cauchy stress tensor at times t and $t + \Delta t$ and the increment in the components with respect to the material frame:

$$^{t+\Delta t}\sigma_{ij} = {}^{t+\Delta t}_{t}Q_{ki} {}^{t+\Delta t}_{t}R_{kl} \left({}^{t+\Delta t}_{t}Q_{lm} {}^{t}\sigma_{mn} {}^{t+\Delta t}_{t}Q_{on} + {}_{t}\Delta\sigma^{M}_{lo} \right) {}^{t+\Delta t}_{t}R_{po} {}^{t+\Delta t}_{t}Q_{pj} \tag{2.11}$$

The proposed stress and the logarithmic strain measures satisfy the requirement of objectivity and lead to a physically consistent application of the usual constitutive equation.

2.4 Strain Measures

The incremental small strain is given by

$$_{t}\Delta\varepsilon_{ij} = \frac{1}{2}({}_{t}\Delta u_{i,j} + {}_{t}\Delta u_{j,i}) \tag{2.12}$$

The incremental Green Lagrange strain is a non-linear function of the displacement

$$_{t}\Delta e_{ij} = \frac{1}{2}({}_{t}\Delta u_{i,j} + {}_{t}\Delta u_{j,i} + {}_{t}\Delta u_{k,i} \, {}_{t}\Delta u_{k,j}) \tag{2.13}$$

These two strain measures occur in the virtual work expression at time $t + \Delta t$ and its transformation to time t respectively. The components of the Green Lagrange strain tensor are invariant under rigid body rotation of the material unlike the small strain components.

The following are the disadvantages of using one of the above measures in a constitutive law:

1. The solution obtained is dependent upon the size of the increment in the Updated Lagrangian formulation unless the increment size is sufficiently small.

2. The components of the strain tensors do not tend to infinite values when the principal stretches tend to zero. Therefore, a constitutive law, which ensures that the appropriate Cauchy stress components tend to negative infinity (as is physically realistic), even though the strain components remain finite, should be used. This difficulty can be avoided by using a strain measure whose components become minus infinity when the principal stretches become zero.

The logarithmic strain measure introduced by Dienes [77] is free of the above disadvantages. The principal incremental logarithmic strain components, which will be used in this work, are defined by

$$_t\Delta\varepsilon_{ij}^L = ln(_t^{t+\Delta t}\lambda_i)\,\delta_{ij} \tag{2.14}$$

where the λ_i are the principal stretches defined by equation (2.4). The logarithmic strain has the following additional advantage in elasto-plastic analysis. A loading test involving elasto-plastic deformation followed by elastic unloading reveals that the slope of the elastic unloading line is the same as that of the initial elastic line only when the true stress and the logarithmic strain measures are used in a constitutive law [80].

2.5 Elastic Constitutive Equation

A constitutive law must satisfy the principle of material frame indifference [76]. The incremental elastic constitutive equation used is the generalized Hooke's law relating the increment in stress components with respect to the material frame and the elastic part ($[\Delta\varepsilon^{eL}]$) of the principal incremental logarithmic strain components:

$$_t\Delta\sigma_{ij}^M = \int_t^{t+\Delta t} C_{ijkl}^E d(_t\Delta\varepsilon_{kl}^{eL}) \tag{2.15}$$

The tensor $[C^E]$ for the isotropic case is given by

$$C_{ijkl}^E = \lambda\,\delta_{ij}\,\delta_{kl} + 2\mu\,\delta_{ik}\,\delta_{jl} \tag{2.16}$$

where λ and μ are Lame's constants.

In case anisotropic behavior is modeled, the tensor C^E has to be evaluated with reference to the directions of the principal stretches.

The stress and strain measures used in a constitutive equation need not necessarily be energy conjugate with each other. However if it is so, the predicted response in a predictor-corrector scheme will be closer to the actual response.

2.6 Elasto-Plastic Constitutive Equation

As stresses developed in a material exceed the yield stress, the elastic constitutive relationship between the stress and strain tensors no longer remains valid. We now develop a relationship between the stress and strain based on the von Mises yield criterion and isotropic hardening.

For an isotropically hardening material, the plastic potential is given by [81]

$$F(\sigma_{ij}, p) = \sigma_{eq}(\sigma_{ij}) - \sigma_y(p) \tag{2.17}$$

note that

$$F = 0 \tag{2.18}$$

represents the yield criterion. The plastic potential F depends on the Cauchy stress tensor σ_{ij} through it's second invariant σ_{eq} called as equivalent stress and defined by

$$\sigma_{eq} = \left(\frac{3}{2}\sigma'_{ij}\,\sigma'_{ij}\right)^{\frac{1}{2}} \tag{2.19}$$

where σ'_{ij} is the deviatoric part of σ_{ij}. Further, F depends on the variable yield stress of the material, σ_y, through a hardening variable p. For the case of strain hardening, p is identified as the equivalent plastic strain ε^p_{eq}, and hence defined as:

$$p = \varepsilon^p_{eq} = \int d\varepsilon^p_{eq} \tag{2.20}$$

where

$$d\varepsilon^p_{eq} = \left(\frac{2}{3}d\varepsilon^p_{ij}\,d\varepsilon^p_{ij}\right)^{\frac{1}{2}} \tag{2.21}$$

Here, $d\varepsilon^p_{ij}$ is the plastic part of the incremental linear strain tensor $d\varepsilon_{ij}$ and the integration in equation (2.20) is to be carried along the particle path. The dependence of σ_y on p (or ε^p_{eq}) is normally approximated by a power law type of relationship

$$\sigma_y - (\sigma_y)_o = K(\varepsilon^p_{eq})^n \tag{2.22}$$

Here, $(\sigma_y)_o$ is the yield stress at zero plastic strain, K is called the hardening coefficient and n is called as the hardening exponent.

The plastic part of incremental linear strain tensor $(d\varepsilon^p_{ij})$ is obtained from the plastic potential using the following relation:

$$d\varepsilon_{ij}^{p} = d\lambda \frac{\partial F}{\partial \sigma_{ij}} \qquad (2.23)$$

where $d\lambda$ is a scalar. This equation is called the flow rule. Differentiation of equation (2.17) with respect to σ_{ij} gives

$$\frac{\partial F}{\partial \sigma_{ij}} = \frac{3}{2\sigma_{eq}} \sigma_{ij}' \qquad (2.24)$$

using this, one can determine $d\lambda$ as:

$$d\lambda = d\varepsilon_{eq}^{p} \qquad (2.25)$$

Further, the hardening relationship and the yield condition can be used to express $d\lambda$ as:

$$d\lambda = \frac{d\sigma_{y}}{H} = \frac{d\sigma_{eq}}{H} \qquad (2.26)$$

where

$$H = \frac{d\sigma_{y}}{d\varepsilon_{eq}^{p}} = Kn(\varepsilon_{eq}^{p})^{n-1} \qquad (2.27)$$

is the slope of the hardening curve. Substitution of equation (2.24) and (2.26) in equation (2.23) leads to the following constitutive equation

$$d\varepsilon_{ij}^{p} = \frac{3}{2} \frac{d\sigma_{eq}}{H\sigma_{eq}} \sigma_{ij}' \qquad (2.28)$$

This constitutive relationship between the deviatoric stress tensor and the plastic part of linear strain tensor is not really convenient for the Updated Lagrangian formulation for which the incremental stress-strain relationship is needed. This can be obtained from equation (2.28) as follows:

$$d\varepsilon_{ij}^{p} = \frac{3}{2} \frac{\sigma_{ij}'}{H\sigma_{eq}} \frac{\partial \sigma_{eq}}{\partial \sigma_{kl}} d\sigma_{kl} \qquad (2.29)$$

Note that, from equations (2.17) and (2.24), we get

$$\frac{\partial \sigma_{eq}}{\partial \sigma_{kl}} = \frac{\partial F}{\partial \sigma_{kl}} = \frac{2}{3\sigma_{eq}} \sigma_{kl}' \qquad (2.30)$$

Substitution of equation (2.30) in equation (2.29) leads to the following incremental plastic stress strain relationship:

$$d\varepsilon_{ij}^{p} = \frac{9\sigma_{ij}' \sigma_{kl}'}{4H\sigma_{eq}^{2}} d\sigma_{kl} \qquad (2.31)$$

The incremental elastic stress strain relationship (equations (2.15)-(2.16)) can now be written as:

$$de^e_{ij} = \frac{1}{E}[-\nu d\sigma_{kk}\delta_{ij} + (1+\nu)d\sigma_{ij}] \tag{2.32}$$

where $d\varepsilon^e_{ij}$ is the elastic part of $d\varepsilon_{ij}$, E is the Young's modulus and ν is the Poisson's ratio. Adding the two relationships, we get

$$d\varepsilon_{ij} = d\varepsilon^e_{ij} + d\varepsilon^p_{ij} \tag{2.33}$$

$$= \left[\frac{-\nu}{E}\delta_{ij}\,\delta_{kl} + \frac{1+\nu}{E}\delta_{ik}\,\delta_{jl} + \frac{9\sigma'_{ij}\sigma'_{kl}}{4H\sigma^2_{eq}}\right]d\sigma_{kl} \tag{2.34}$$

This is the incremental elasto-plastic stress strain relationship needed in the Updated Lagrangian formulation. However, it is the following inverse relationship which is more useful:

$$d\sigma_{ij} = C^{EP}_{ijkl}\,d\varepsilon_{kl} \tag{2.35}$$

where

$$C^{EP}_{ijkl} = 2\mu\left(\delta_{ik}\,\delta_{jl} + \frac{\nu}{1-2\nu}\delta_{ij}\,\delta_{kl} - \frac{9\mu\sigma'_{ij}\sigma'_{kl}}{2(3\mu+H)\sigma^2_{eq}}\right) \tag{2.36}$$

and μ is one of the Lame's constant (also called shear modulus) appearing in equation (2.16).

Note that the stress increment appearing in equation (2.35) must be an objective stress increment in the sense that $d\sigma_{ij}$ must reduce to a zero tensor in the event of the increment being a pure rigid rotation. The incremental objective stress measure to be used in the present work has been described in section 2.3.

The relationship (2.35) has been derived assuming the increment size to be small and suing the incremental linear strain tensor as the strain measure. When a large size increment is to be used along with the incremental logarithmic strain measure (defined in section 2.4), the derivation is similar. The relationship (2.35), when the stress and strain measures are replaced respectively by the incremental objective stress measure (of section 2.3) and the incremental logarithmic strain measure (of section 2.4), takes the following form with respect to the material frame.

$$_t\Delta\sigma^M_{ij} = \int_t^{t+\Delta t} {}^tC^{EP}_{ijkl}\,d(_t\Delta\varepsilon^L_{kl}) \tag{2.37}$$

where

$${}^tC^{EP}_{ijkl} = 2\mu\left(\delta_{ik}\,\delta_{jl} + \frac{\nu}{1-2\nu}\delta_{ij}\,\delta_{kl} - \frac{9\mu\,{}^t\sigma'_{ij}\,{}^t\sigma'_{ij}}{2(3\mu + Kn\,(^t\varepsilon^p_{eq})^{n-1})\,{}^t\sigma^2_{eq}}\right) \tag{2.38}$$

Here, H has been replaced by the expression (2.27) and the left superscript t has been added to make it explicit that these quantities are to be evaluated at that time.

2.7   Incremental Updated Lagrangian Formulation Cartesian

The objective of the Updated Lagrangian formulation is to establish static equilibrium in the configuration at time $t + \Delta t$ when all static variables at time t are known. The principle of virtual work requires that

$$\int_{t+\Delta t_V} {}^{t+\Delta t}\sigma_{ij}\delta({}^{t+\Delta t}\varepsilon_{ij})d^{t+\Delta t}V = {}^{t+\Delta t}R \tag{2.39}$$

where

${}^{t+\Delta t}\sigma_{ij}$ = Cartesian component of the Cauchy stress tensor at time $t + \Delta t$,

$$\delta^{t+\Delta t}\varepsilon_{ij} = \tfrac{1}{2}\left(\frac{\partial \delta^{t+\Delta t}u_i}{\partial^{t+\Delta t}x_j} + \frac{\partial \delta^{t+\Delta t}u_j}{\partial^{t+\Delta t}x_i}\right),$$

$\delta^{t+\Delta t}u_i$ = Cartesian component of the virtual displacement at time $t + \Delta t$,

${}^{t+\Delta t}x_i$ = Cartesian coordinate of a material point at time $t + \Delta t$,

${}^{t+\Delta t}V$ = volume at time $t + \Delta t$ and

$$^{t+\Delta t}R = \int_{t+\Delta t_{S_f}} {}^{t+\Delta t}f_i\,\delta^{t+\Delta t}u_i\,d^{t+\Delta t}S \tag{2.40}$$

where

${}^{t+\Delta t}f_i$ = Cartesian component of external traction at time $t + \Delta t$

${}^{t+\Delta t}S_f$ = Surface at time $t + \Delta t$ with traction specified.

The main difficulty in the application of equation (2.39) is that the configuration at time $t + \Delta t$ is unknown. An elegant way of formulating the problem is given by Bathe [82]. The virtual work expression at time $t + \Delta t$ is transformed to an integral over the volume at time t by using the second Piola-Kirchoff stress and Green Lagrange strain measures, which are energy conjugate to each other, and the principle of conservation of mass. it is assumed that the external load term (2.40) is deformation independent for the formulation of the governing equation. The expression (2.39) after the transformation becomes

$$\int_{t_V} {}^{t+\Delta t}_t S_{ij}\,\delta({}^{t+\Delta t}_t e_{ij})d^t V = {}^{t+\Delta t}R \tag{2.41}$$

The Green-Lagrange strain tensor ${}^{t+\Delta t}_t e_{ij}$ is defined by

$$^{t+\Delta t}_t e_{ij} = \frac{1}{2}({}^{t+\Delta t}_t u_{i,j} + {}^{t+\Delta t}_t u_{j,i} + {}^{t+\Delta t}_t u_{k,i}\,{}^{t+\Delta t}_t u_{k,j}) \tag{2.42}$$

where ${}^{t+\Delta t}_t u_{i,j}$ denotes the derivative of ${}^{t+\Delta t}u_i$ with respect to ${}^t x_j$.

The second Piola-Kirchoff stress tensor can be decomposed as

$$^{t+\Delta t}_t S_{ij} = {}^t_t S_{ij} + {}_t \Delta S_{ij} = {}^t \sigma_{ij} + {}_t \Delta S_{ij} \tag{2.43}$$

Since

$$\delta(^{t+\Delta t}u_i) = \delta(^tu_i +_t \Delta u_i) = \delta(_t\Delta u_i) \tag{2.44}$$

the virtual Green-Lagrange strain tensor can be decomposed as

$$\delta(^{t+\Delta t}_t e_{ij}) = \delta(_t\Delta e_{ij}) = \delta(_t\Delta\varepsilon_{ij} +_t \Delta\eta_{ij}) \tag{2.45}$$

where

$$_t\Delta\varepsilon_{ij} = \frac{1}{2}(_t\Delta u_{i,j} +_t \Delta u_{j,i}) \tag{2.46}$$

$$_t\Delta\eta_{ij} = \frac{1}{2}(_t\Delta u_{k,i} +_t \Delta u_{k,j}) \tag{2.47}$$

Therefore, equation (2.41) can be written with incremental decomposition as

$$\int_{tV} \Delta S_{ij}\delta(_t\Delta\varepsilon_{ij})d^tV + \int_{tV} \Delta S_{ij}\,\delta(_t\Delta\eta_{ij})d^tV+$$

$$\int_{tV} {}^t\sigma_{ij}\delta(_t\Delta\eta_{ij})d^tV + \int_{tV} {}^t\sigma_{ij}\delta(_t\Delta\varepsilon_{ij})d^tV =^{t+\Delta t} R \tag{2.48}$$

The above equation is linearized by neglecting the second integral, which is a higher order term, and approximating $_t\Delta S_{ij}$ as $^tC^{EP}_{ijkl}\,\Delta\varepsilon_{kl}$:

$$\int_{tV} {}^tC^{EP}_{ijkl}\,_t\Delta\varepsilon_{kl}\,\delta(_t\Delta\varepsilon_{ij})d^tV + \int_{tV} {}^t\sigma_{ij}\,\delta(_t\Delta\eta_{ij})d^tV$$

$$+ \int_{tV} {}^t\sigma_{ij}\,\delta(_t\Delta\varepsilon_{ij})d^tV = {}^{t+\Delta t}R \tag{2.49}$$

The linearized equation, when solved, will yield only approximate displacement, strain and stress fields. The approximate quantities are denoted by a right superscript (1). The error to the approximation involved is calculated from equation (2.39) as

$$Error =^{t+\Delta t} R - \int_{t+\Delta tV^{(1)}} {}^{t+\Delta t}\sigma^{(1)}_{ij}\delta(^{t+\Delta t}\varepsilon^{(1)}_{ij})d^{t+\Delta t}V^{(1)} \tag{2.50}$$

This error is generally minimized by an iterative predictor-corrector scheme described in section 2.11.2.

The next section discusses the finite element formulation of the governing equation (2.49)

2.8 Finite Element Formulation

2.8.1 Matrix Notation

Matrix notation is used in the development of the finite element equations for the convenience of computer implementation.

For the axisymmetric case, the components of the tensors, $_t\Delta\varepsilon$, $_t\Delta\eta$ and $_t\Delta\varepsilon^L$ are represented in array form as follows:

$$_t\{\Delta\varepsilon\}^T = \{_t\Delta\varepsilon_{rr}, {}_t\Delta\varepsilon_{zz}, 2_t\Delta\varepsilon_{rz}, {}_t\Delta\varepsilon_{\theta\theta,}\} \tag{2.51}$$

$$_t\{\Delta\eta\}^T = \{_t\Delta u_{r,r}, {}_t\Delta u_{r,z}, {}_t\Delta u_{z,r}, {}_t\Delta u_{z,z}, \frac{_t\Delta u_r}{r^t}\} \tag{2.52}$$

$$_t\{\Delta\varepsilon^L\}^T = \{_t\Delta\varepsilon^L_{rr}, {}_t\Delta\varepsilon^L_{zz}, {}_t\Delta\varepsilon^L_{rz}, {}_t\Delta\varepsilon^L_{\theta\theta,}\} \tag{2.53}$$

The components of all stress tensors are written as arrays with respective components placed in the following manner:

$$\{\sigma\}^T = \{\sigma_{rr}, \sigma_{zz}, \sigma_{rz}, \sigma_{\theta\theta}\} \tag{2.54}$$

Two matrix forms of the tensor $^tC^{EP}_{ijkl}$ (given by equation (2.38)) are needed:
1. $^t[C^{EP}]'$ for the constitutive relationship : $_t\{\Delta S\} = {}^t[C^{EP}]' \; _t\{\Delta\varepsilon\}$,
2. $^t[C^{EP}]$ for the constitutive relationship : $_t\{\Delta\sigma^M\} = {}^t[C^{EP}] \; _t\{\Delta\varepsilon^L\}$.

They are given by

$$^t[C^{EP}]' = \left([C^{E'}] - \frac{[C^{E'}]^t\{a\}^t\{a\}^T[C^{E'}]}{^tH +{}^t\{a\}^T[C^{E'}]^t\{a\}}\right) \tag{2.55}$$

$$^t[C^{EP}] = \left([C^E] - \frac{[C^E]^t\{a\}^t\{a\}^T[C^E]}{^tH +{}^t\{a\}^T[C^E]^t\{a\}}\right) \tag{2.56}$$

In the above equations,

$$^t\{a\} = \frac{3}{2^t\sigma_{eq}}{}^t\{\sigma'\} \tag{2.57}$$

and the array $^t\{\sigma'\}$ represents the deviatoric part of the Cauchy stress at time t.

For an isotropic material, the matrices $[C^{E'}]$ and $[C^E]$ for the axisymmetric case are given by

$$[C^{E'}] = \frac{E}{(1+\nu)(1-2\nu)}\begin{bmatrix} 1-\nu & \nu & 0 & 0 \\ \nu & 1-\nu & 0 & \nu \\ 0 & 0 & \frac{1-2\nu}{2} & 0 \\ \nu & \nu & 0 & 1-\nu \end{bmatrix} \tag{2.58}$$

$$[C^E] = \frac{E}{(1+\nu)(1-2\nu)} \begin{bmatrix} 1-\nu & \nu & 0 & 0 \\ \nu & 1-\nu & 0 & \nu \\ 0 & 0 & 1-2\nu & 0 \\ \nu & \nu & 0 & 1-\nu \end{bmatrix} \qquad (2.59)$$

Equation (2.49) can be written in the following form owing to the symmetries in $^tC^{EP}$, $_t\{\Delta\varepsilon\}$, $_t\{\Delta\eta\}$ and $^t\sigma$:

$$\int_{t_V} \delta(_t\{\Delta\varepsilon\}^T)^t[C^{EP'}]_t\{\Delta\varepsilon\}d^tV + \int_{t_V} \delta(_t\{\Delta\eta\}^T)^t[T]_t\{\Delta\eta\}d^tV +$$

$$\int_{t_V} \delta(_t\{\Delta\varepsilon\}^T)^t\{\sigma\}d^tV = {}^{t+\Delta t}R \qquad (2.60)$$

where the matrix $^t[T]$ is given by

$$^t[T] = \begin{bmatrix} ^t\sigma_{rr} & ^t\sigma_{rz} & 0 & 0 & 0 \\ ^t\sigma_{zr} & ^t\sigma_{zz} & 0 & 0 & 0 \\ 0 & 0 & ^t\sigma_{rr} & ^t\sigma_{rz} & 0 \\ 0 & 0 & ^t\sigma_{zr} & ^t\sigma_{zz} & 0 \\ 0 & 0 & 0 & 0 & ^t\sigma_{\theta\theta} \end{bmatrix} \qquad (2.61)$$

2.8.2 Finite Element Equations

The domain is discretized into a number of elements and the incremental displacement field is approximated over each element by

$$_t\{\Delta u\} = \left\{ \begin{array}{c} _t\Delta u_r \\ _t\Delta u_z \end{array} \right\} = {}^t[\Phi]_t\{\Delta u\}^e \qquad (2.62)$$

where the element incremental displacement vector $_t\{\Delta u\}^e$ for an n-noded element is given by

$$_t\{\Delta u\}^{e^T} = \{_t\Delta u_r^1, \ _t\Delta u_z^1, \ \ldots\ldots\ldots,_t \Delta u_r^n,_t \Delta u_z^n\} \qquad (2.63)$$

The quantities $_t\Delta u_r{}^i$, $_t\Delta u^i{}_z$ stand for the unknown incremental displacements of node i in r and z directions respectively and the matrix $^t[\Phi]$ is defined by

$$^t[\Phi] = \begin{bmatrix} ^t\{\Phi_1\}^T \\ ^t\{\Phi_2\}^T \end{bmatrix} \qquad (2.64)$$

where

$$^t\{\Phi_1\}^T = \{ ^tN_1, \ 0, \ ^tN_2, \ 0, \ \ldots, \ ^tN_n, \ 0 \}$$

$$^t\{\Phi_1\}^T = \{ 0, \ ^tN_1, \ 0, \ ^tN_2, \ \ldots, \ 0, \ ^tN_n \} \qquad (2.65)$$

The ^tN_i, which are functions of $(^tr, ^tz)$ are called shape functions. The number of nodes and the corresponding shape functions are chosen on the basis of convergence criteria. For the problem under consideration, 8-noded serendipity element is used.

The strain field is expressed in terms of the nodal displacements by differentiating (2.62) and using the expression (2.46) and (2.47). This leads to

$$_t\{\Delta\varepsilon\} = ^t[B_L]_t\{\Delta u\}^e \tag{2.66}$$

$$_t\{\Delta\eta\} = ^t[B_N]_t\{\Delta u\}^e \tag{2.67}$$

where

$$^t[B_L] = \begin{bmatrix} ^t\{\Phi_1\}_{,r}^T \\ ^t\{\Phi_2\}_{,z}^T \\ ^t\{\Phi_2\}_{,r}^T + ^t\{\Phi_1\}_{,z}^T \\ ^t\{\Phi_1\}^T/^tr \end{bmatrix} \tag{2.68}$$

and

$$^t[B_N] = \begin{bmatrix} ^t\{\Phi_1\}_{,r} \\ ^t\{\Phi_1\}_{,z} \\ ^t\{\Phi_2\}_{,r} + ^t\{\Phi_2\}_{,z} \\ ^t\{\Phi_1\}/^tr \end{bmatrix} \tag{2.69}$$

Using equations (2.62), (2.66) and (2.67), the contribution to the integral (2.60) over a typical element e with volume V^e is

$$\delta\left(_t\{\Delta u\}^{e^T}\right) \left(\int_{tV^e} ^t[B_L]^T \, ^t[C^{EP'}] \, ^t[B_L] \, d^tV^e\right) _t\{\Delta u\}^e +$$

$$\delta\left(_t\{\Delta u\}^{e^T}\right) \left(\int_{tV^e} ^t[B_N]^T \, ^t[T] \, ^t[B_N] d^tV^e\right) _t\{\Delta u\}^e +$$

$$\delta\left(_t\{\Delta u\}^{e^T}\right) \left(\int_{tV^e} ^t[B_L]^T \, ^t[\sigma] \, d^tV^e\right) = \delta\left(_t\{\Delta u\}^{e^T}\right) {}^{t+\Delta t}\{F\}^e \tag{2.70}$$

The contribution to the term $^{t+\Delta t}R$ is expressed in terms of the elemental external force vector $^{t+\Delta t}\{F\}^e$ using a standard procedure. Since the variation in the displacement vector is arbitrary, the above equation can be written as

$$
{}^{t}[K]^{e}{}_{t}\{\Delta u\}^{e} + {}^{t}\{f\}^{e} = {}^{t+\Delta t}\{F\}^{e} \tag{2.71}
$$

where the elemental stiffness matrix ${}^{t}[K]^{e}$ is given by

$$
{}^{t}[K]^{e} = {}^{t}[K_{L}]^{e} + {}^{t}[K_{NL}]^{e} \tag{2.72}
$$

$$
{}^{t}[K_{L}]^{e} = \int_{{}^{t}V^{e}} {}^{t}[B_{L}]^{T}\, {}^{t}[C^{EP'}]\, {}^{t}[B_{L}]\, d^{t}V^{e} \tag{2.73}
$$

$$
{}^{t}[K_{NL}]^{e} = \int_{{}^{t}V^{e}} {}^{t}[B_{N}]^{T}\, {}^{t}[T]\, {}^{t}[B_{N}]\, d^{t}V^{e} \tag{2.74}
$$

and the elemental internal force vector is

$$
{}^{t}\{f\}^{e} = \int_{{}^{t}V^{e}} {}^{t}[B_{L}]^{T}\, {}^{t}[\sigma]\, d^{t}V^{e} \tag{2.75}
$$

The elemental stiffness matrix ${}^{t}[K]^{e}$ along with the elemental force vector ${}^{t}\{f\}^{e}$ and ${}^{t+\Delta t}\{F\}^{e}$ are assembled to obtain the global equation.

$$
{}^{t}[K]_{t}\{\Delta u\} + {}^{t}\{f\} = {}^{t+\Delta t}\{F\} \tag{2.76}
$$

Decomposing ${}^{t+\Delta t}\{F\}$, equation (2.76) can be written as

$$
{}^{t}[K]_{t}\{\Delta u\} + {}^{t}\{f\} = {}^{t}\{F\} + {}_{t}\{\Delta F\} \tag{2.77}
$$

Here, ${}^{t}\{F\}$ is the (global) external force vector at time t and ${}_{t}\{\Delta F\}$ is the (global) incremental force vector from time t to $t + \Delta t$. In Updated Lagrangian formulation, it is assumed that the equilibrium equations are satisfied exactly at time t. Thus

$$
{}^{t}\{f\} = {}^{t}\{F\} \tag{2.78}
$$

$$
{}^{t}[K]_{t}\{\Delta u\} = {}_{t}\{\Delta F\} \tag{2.79}
$$

This equation is solved to obtain the incremental displacement vector ${}_{t}\{\Delta u\}$.

2.8.3   Static condensation scheme

When the Gauss elimination method is applied to the problems consisting of contact boundary conditions after incorporating them, there is a possibility that the pivot may become zero. Storage of the coefficient matrix in the full form is also not desirable. Since the contact condition needs to be applied in an iterative manner, solving the full storage equations in all the iterations takes an enormously large amount of time, especially when the number of degrees of freedom is high. To reduce the solution time, it is desirable to condense the

coefficient matrix and the right side vector to the size involving only those degree of freedom to which the contact boundary condition is to be applied. This condensation procedure is described in the next paragraph.

First the total nodes are divided into two categories. The nodes at which contact condition is to be applied are called the nodes of type 2. The rest of the nodes are called as nodes of type 1. To facilitate the condensation, the nodes are numbered in such a manner that the nodes of type 1 are numbered first and then the nodes of type 2 are numbered. Then the essential boundary conditions (i.e, the boundary conditions on the incremental displacement vector, which is the primary variable in this case) for the nodes of type 1 are applied to equation (2.79). The essential boundary conditions of the forging process are described in section 2.9.

Next, these equations are partitioned as follows[1]:

$$\begin{bmatrix} [K_{11}] & [K_{12}] \\ [K_{21}] & [K_{22}] \end{bmatrix} \left\{ \begin{array}{c} \{\Delta u_1\} \\ \{\Delta u_2\} \end{array} \right\} = \left\{ \begin{array}{c} \{\Delta F_1\} \\ \{\Delta F_2\} \end{array} \right\} \tag{2.80}$$

where $\{\Delta u_1\}$ denotes the incremental displacement vector corresponding to the nodes of type 1 and $\{\Delta u_2\}$ contains the incremental displacements of the nodes of type 2. Equation (2.80) can be separated as follows:

$$[K_{11}]\{\Delta u_1\} + [K_{12}]\{\Delta u_2\} = \{\Delta F_1\}, \tag{2.81}$$

$$[K_{21}]\{\Delta u_1\} + [K_{22}]\{\Delta u_2\} = \{\Delta F_2\}. \tag{2.82}$$

solving for $\{\Delta u_1\}$ from equation (2.81), we get

$$\{\Delta u_1\} = [K_{11}]^{-1}(\{\Delta F_1\} - [K_{12}]\{\Delta u_2\}). \tag{2.83}$$

Substitution of this expression for $\{\Delta u_1\}$ in equation (2.82) and rearrangement of the resulting equation leads to the condensed set of approximate equilibrium equations:

$$[\widehat{K}]\{\Delta \widehat{u}\} = \{\Delta \widehat{F}\} \tag{2.84}$$

where

$$[\widehat{K}] = [K_{22}] - [K_{21}][A], \tag{2.85}$$

$$\{\Delta \widehat{u}\} = \{\Delta u_2\}, \tag{2.86}$$

$$\{\Delta \widehat{F}\} = \{\Delta F_2\} - [K_{21}][B], \tag{2.87}$$

---

[1]In this section, the superscripts/subscripts denoting time have been omitted for the sake of convenience.

$$[A] = [K_{11}]^{-1}[K_{12}], \qquad (2.88)$$

$$\{B\} = [K_{11}]^{-1}\{\Delta F_1\}, \qquad (2.89)$$

The number of equations in the condensed set (2.84) is equal to the number of degrees of freedom of type 2. The coefficient matrix $[\widehat{K}]$ and the right side vector $\{\widehat{F}\}$ are evaluated from equations (2.85-2.89) using the partitioned matrices and vectors of equation (2.80). Note that while evaluating $[A]$ and $[B]$, it is not necessary to invert the matrix $[K_{11}]$. Instead, one can solve the following equations by the Gauss elimination method:

$$[K_{11}][A] = [K_{12}], \qquad (2.90)$$

$$[K_{11}]\{B\} = \{\Delta F_1\}, \qquad (2.91)$$

To reduce the computational time further, one can store the upper triangular from of $[K_{11}]$. In this way, one can obtain columns of $[A]$ by performing the Gauss elimination and back substitution operations on the corresponding columns of $[K_{12}]$. The vector $\{B\}$ is obtained in similar fashion by performing the Gauss elimination and back substitution operations on the vector $\{\Delta F_1\}$.

2.8.4 Determination of Stresses

The evaluation of the stress components (at the Gauss points of the elements) is done by the following stepwise procedure:

1. Calculate the relative deformation gradient $^{t+\Delta t}_{t}[F]$:

$$^{t+\Delta t}_{t}[F] = \begin{bmatrix} 1 + \frac{\partial (_t\Delta u_r)}{\partial {}^t r} & 0 & \frac{\partial (_t\Delta u_r)}{\partial {}^t z} \\ 0 & 1 + \frac{_t\Delta u_r}{{}^t r} & 0 \\ \frac{\partial (_t\Delta u_z)}{\partial {}^t r} & 0 & 1 + \frac{\partial (_t\Delta u_z)}{\partial {}^t z} \end{bmatrix} \qquad (2.92)$$

It should be noted that the position vector $^t x$ corresponds to the equilibrium position.

2. Decompose the relative deformation gradient as $^{t+\Delta t}_{t}[F] = {}^{t+\Delta t}_{t}[R]\, {}^{t+\Delta t}_{t}[U]$ and determine $^{t+\Delta t}_{t}[Q]$ and $^{t+\Delta t}_{t}[U^p]$ using equation (2.3).

3. Determine the principal incremental logarithmic strain $_t\{\Delta\varepsilon^L\}$ using equation (2.14).

4. Calculate $_t\{\Delta\sigma^M\}$ using equation (2.37). The integration of the constitutive equation is performed using the Euler forward technique described below.

5. Use equation (2.11) to calculate the Cauchy stress components at time $t + \Delta t$.

2.8.5 Integration of the Constitutive Equation

Different techniques exist for the integration of the constitutive equation. A simple and robust technique is the Euler forward integration scheme described below.

Assume that the principal incremental strain components have been calculated and the state of the Gauss point at time t (elastic or plastic) is known.

• If the state at time t is elastic,

1. Calculate the stress increment assuming elastic behavior

$$_t\{\Delta\sigma^M\} = [C^E] \, _t\{\Delta\varepsilon^L\}.$$

2. Calculate $^{t+\Delta t}\{\sigma\}$ using (2.11).

3. Determine $^t\sigma_{eq}$ and $^{t+\Delta t}\sigma_{eq}$ using (2.19).

4. If $^{t+\Delta t}\sigma_{eq} \leq {}^{t+\Delta t}\sigma_y$, then elastic behavior holds, or if $^{t+\Delta t}\sigma_{eq} = {}^t\sigma_{eq}$ the Gauss point is neutrally loaded. **Return**.

5. If $^{t+\Delta t}\sigma_{eq} \; ¿ \; {}^{t+\Delta t}\sigma_y$, a transition from elastic to plastic has occurred. Calculate the

$$Ratio = \frac{({}^{t+\Delta t}\sigma_y - {}^t\sigma_{eq})}{({}^{t+\Delta t}\sigma_{eq} - {}^t\sigma_{eq})},$$

Change the state to plastic and use the sub-incrementation method. In this method, the stress components with respect to the material frame are updated after each sub increment by the increment in stress components corresponding to the elasto-plastic strain sub-increment.

The $[C^{EP}]$ corresponding to the last updated state is used:

$$^{t+\Delta t}\{\sigma^M\}^{(i)} = {}^{t+\Delta t}\{\sigma^M\}^{(i-1)} + {}^{t+\Delta t}[C^{EP}]^{(i-1)} \, d_t\{\Delta\varepsilon^L\} \text{ for } i = 1, n$$
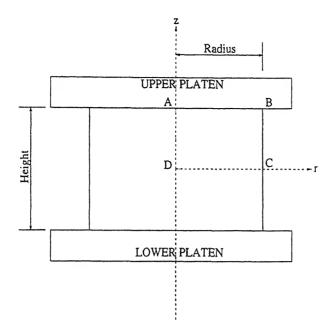
where

Figure 2.2: Domain of the Problem

$$d_t\{\Delta\varepsilon^L\} = \frac{(1-Ratio)_t\{\Delta\varepsilon^L\}}{n},$$

$$^{t+\Delta t}\{\sigma^M\}^{(0)} = \,^t\{\sigma^M\} + \text{Ratio}[C^E]_t\,\{\Delta\varepsilon^L\},$$

$$^{t+\Delta t}\{C^{EP}\}^{(0)} = [C^{EP}] \text{ evaluated at } ^{t+\Delta t}\{\sigma^M\}^{(0)}$$

Use equation (2.10) to find $^{t+\Delta t}\sigma_{ij}$. **Return.**

- If the state at time t is plastic, the sub increment method described in (5) above is applied with *Ratio* set to zero.

This describes the Euler forward scheme for the elasto-plastic model described in section 2.6

2.9 Boundary Conditions for Axisymmetric Forging of Cylindrical Disc

Figure 2.2 shows the domain of the problem. Due to symmetry, only the upper half of the workpiece is used for analysis. The boundary conditions for the domain of this problem are discussed below.

2.9.1 The Workpiece-Die Interface (AB)

As stated in section 1.2 of chapter 1, the friction at the workpiece die interface is modelled by the Coulomb's law. Therefore, a node of the workpiece at the interface either sticks to the die or slips relative to the die depending on the magnitude of the stress in r-direction and the coefficient of friction μ. Therefore, the boundary condition in r-direction can be stated as:

$$\left|{}^{t+\Delta t}t_r\right| - \mu\left|{}^{t+\Delta t}t_z\right| = 0 \quad if \quad \left|{}^{t+\Delta t}t_r\right| \geq \mu\left|{}^{t+\Delta t}t_z\right| \tag{2.93}$$

or

$$_t\Delta u_r = 0 \qquad if \quad \left|{}^{t+\Delta t}t_r\right| < \mu\left|{}^{t+\Delta t}t_z\right| \tag{2.94}$$

Since both t_r and t_z are negative, the first condition can be stated as

$$^{t+\Delta t}t_r - \mu{}^{t+\Delta t}t_z = 0 \quad if \quad \left|{}^{t+\Delta t}t_r\right| \geq \mu\left|{}^{t+\Delta t}t_z\right| \tag{2.95}$$

Since nodal forces are proportional to the stress components, this condition can be expressed in terms of the nodal forces also. In fact, this is the form, which is convenient in finite element formulation. Thus, the boundary condition in r-direction becomes:

Natural boundary condition:

$$^{t+\Delta t}F_r - \mu{}^{t+\Delta t}F_z = 0 \quad if \quad \left|{}^{t+\Delta t}F_r\right| \geq \mu\left|{}^{t+\Delta t}F_z\right| \tag{2.96}$$

or

Essential boundary condition:

$$_t\Delta u_r = 0 \qquad if \quad \left|{}^{t+\Delta t}F_r\right| < \mu\left|{}^{t+\Delta t}F_z\right| \tag{2.97}$$

Since this is a displacement control problem, z-component of incremental displacement vector is specified at the interface. Thus, the boundary condition in z-direction is:

Essential boundary condition:

$$_t\Delta u_z = \text{specified} \tag{2.98}$$

2.9.2 The Free Surfaces (BC)

These boundaries are traction free surfaces. Therefore, the boundary conditions on BC are,

Natural boundary conditions:

$$_t\Delta F_r = 0, \; _t\Delta F_z = 0. \tag{2.99}$$

Here, $_t\Delta F_r$ and $_t\Delta F_z$ are the components of the incremental force vector.

2.9.3 The Plane of Symmetry (CD)

Because of symmetry, z-component of incremental displacement vector and r-component of incremental traction/force vector are zero. Thus the boundary conditions on CD are:

Natural boundary condition:

$$_t\Delta F_r = 0. \tag{2.100}$$

Essential boundary condition:

$$_t\Delta u_z = 0. \tag{2.101}$$

2.9.4 The Axis of Symmetry (DA)

Again, due to symmetry, r-component of incremental displacement vector and z-component of incremental traction/force vector are zero.

Natural boundary condition:

$$_t\Delta F_z = 0. \tag{2.102}$$

Essential boundary condition:

$$_t\Delta u_r = 0. \tag{2.103}$$

2.10 Damage Formulation

A continuum damage mechanics criterion proposed by Dhar [46,75] is used to predict microcrack initiation in the present work. This has been discussed in section 1.2.2. Implementation of this criterion is discussed below.

2.10.1 Implementation of Dhar's [46,75] Model

In this model, damage D is identified as an area void fraction at a point in a plane. It is defined by equation (1.21).

The damage growth law which gives rate of change of D is given by equation (1.24), which is reproduced below:

$$\dot{D} = C_D\dot{\bar{\varepsilon}} + (a_1 + a_2 D)(-Y)\dot{\bar{\varepsilon}} \tag{2.104}$$

where $-Y$ is the rate at which the elastic energy releases during the damage growth at constant stress. For an isotropic material, it is given by [47]

$$-Y = \frac{\bar{\sigma}^2}{2E\,(1-D)^2}\, f(\frac{\sigma_m}{\bar{\sigma}}) \qquad (2.105)$$

where

$$f(\frac{\sigma_m}{\bar{\sigma}}) = \frac{2(1+\nu)}{3} + 3(1-2\nu)\,(\frac{\sigma_m}{\bar{\sigma}})^2 \qquad (2.106)$$

As already described in section 1.2.2, the constants fitting equation (2.104) are found for SAE 1090 steel as:

$C_D = 1.898 \times 10^{-2}$, $a_1 = 9.8 \times 10^{-4}$ MPa^{-1} and $a_2 = 1.84$ MPa^{-1}.

Equation (2.104) can be written to give the value of increment in D at a point in the domain as

$$_t\Delta D = C_D\,_t\Delta\bar{\varepsilon} + (a_1 + a_2\,^t D)\,(-^{t+\Delta t}Y)\,_t\Delta\bar{\varepsilon} \qquad (2.107)$$

where

$$-(^{t+\Delta t}Y) = \frac{^{t+\Delta t}\bar{\sigma}^2}{2E\,(1-\,^t D)^2}\, f(\frac{^{t+\Delta t}\sigma_m}{^{t+\Delta t}\bar{\sigma}}) \qquad (2.108)$$

where function f is as defined in equation (2.106).

Since, the strains and stresses are calculated at the Gauss points, value of ΔD can be found at every Gauss point in an element. This can then be used to determine damage growth variable D at time $t + \Delta t$.

$$^{t+\Delta t}D = \,^t D + \,_t\Delta D \qquad (2.109)$$

The value of D is taken as zero at the beginning. Thus, a damage distribution in the domain can be obtained. The crack initiates wherever the value of D reaches the critical limit of 0.05 (for SAE 1090 steel).

2.11   Solution Procedure

Equation (2.84) represents only an approximate equilibrium equation at time $t + \Delta t$ (the approximation is mostly due to the linearisation and simplification involved in the steps between equations (2.48) and (2.49). A solution of such an approximate equation may involve a significant amount of error and depending on incremental displacement step, it may become unstable. Therefore, it is necessary to modify equation (2.84) to turn it into iterative problem capable of providing a solution with desirable accuracy. Amongst various iterative techniques [78], the modified Newton-Raphson algorithm is the most effective as it offers fast convergence with less computation. This algorithm is described in section (section 2.11.2).

As stated in section 1.2 of chapter 1, in the present problem, the friction at the workpiece-die interface is modelled by the Coulomb friction law. The corresponding friction condition is given by equations (2.96-2.97), which can be applied only in an iterative fashion. Thus there are two sets of iterations in the solution procedure of the present problem. First, for the specified incremental force/displacement, the friction iterations are carried out to determine the status (sticking or slipping) of the interface nodes. This algorithm is described in section 2.11.1. Then, corresponding to this status, modified Newton-Raphson iterations are carried out to minimize the error arising out of linearisation and simplification of the equilibrium equation.

Forging is a displacement control problem i.e the deformation is controlled by a specified displacement (at the workpiece-die interface) rather than by a specified traction. In such problems the rate of convergence of the modified Newton-Raphson iterative scheme is usually slow. To accelerate the rate of convergence, the arc length method is used in conjunction with the modified Newton-Raphson scheme. This scheme is explained in section 2.11.3.

Finally, the numerical integration scheme for the elemental coefficient matrices and right side vectors and some divergence-handling procedures for the modified Newton-Raphson scheme are presented in sections 2.11.4 and 2.11.5 respectively.

2.11.1 Friction Algorithm

This section describes the iterative procedure to apply the friction boundary conditions (eq. (2.96-2.97)) to the linearized and condensed set of finite element equations (2.84). The iterative algorithm is as follows:

(I) First step:
1. In the first iteration, it is assumed that all the interface nodes are sticking. Thus, the boundary condition given by the equation (2.97) is applied to all nodes.

2. Next these equations are solved to obtain $\{_t\Delta u_2\}$. The vector $\{_t\Delta u_1\}$ is determined from equation (2.83). Thus the whole incremental displacement vector $\{_t\Delta u\}$ is known.

3. Then, the reactions are found by multiplying the original coefficient matrix with the incremental displacement vector.

4. At the end of the contact iteration, the slipping nodes at the interface are identified using the condition
$$\left|^{t+\Delta t}F_r\right| \geq \mu \left|^{t+\Delta t}F_z\right|.$$

(II) Second step:

1. Now the condition (2.96) is applied to all the slipping nodes. This is done as follows:

If i is the type 2 node number of a slipping node, then application of condition (2.96) to equation (2.84) means replacing $(2i-1)^{th}$ row of ${}^t[\widehat{K}]$ by the combination:

${}^t\widehat{K}_{2i-1,j} - \mu\, {}^t\widehat{K}_{2i,j}$ for $j=1$, number of degrees of freedom of type 2

and setting $(2i-1)^{th}$ row of ${}^t[\Delta\widehat{F}]$ to zero.

2. Then the resulting equations are solved to find $\{{}_t\Delta u_2\}$. The vector $\{{}_t\Delta u_1\}$ is found as before.

3. Now the reactions are found by the method described above.

4. Finally, a check is made to find whether any additional nodes are slipping by using the condition

$$\left|{}^{t+\Delta t}F_r\right| \geq \mu\left|{}^{t+\Delta t}F_z\right|.$$

(III) Further steps:

The second step is repeated till the condition $\left|{}^{t+\Delta t}F_r\right| < \mu\left|{}^{t+\Delta t}F_z\right|$ is satisfied at all the nodes.

2.11.2   Modified Newton-Raphson Scheme

The condensed set of approximate equilibrium equations (2.84), when the superscript/superscript denoting the time are restored, takes the form:

$$ {}^t[\widehat{K}]_t\{\Delta\widehat{u}\} =_t \{\Delta\widehat{F}\} \tag{2.110} $$

The modified Newton-Raphson iterative scheme is used to convert this problem into an iterative problem to improve the accuracy of the solution. This algorithm can be stated as follows.

Solve

$$ {}^t[\widehat{K}]_t\{\Delta\widehat{u}\}^{(i)} =_t \{\Delta\widehat{R}\}^{(i-1)} \tag{2.111} $$

where

$$ {}_t\{\widehat{R}\}^{(i-1)} =^{t+\Delta t}\{\widehat{F}\}^{(i-1)} -^{t+\Delta t}\{\widehat{f}\}^{(i-1)} \tag{2.112} $$

$$ {}_t\{\widehat{R}\}^{(0)} =_t \{\Delta\widehat{F}\} \tag{2.113} $$

till the convergence criterion

$$\frac{\left\|{}_t\{R\}^{(i)}\right\|}{\left\|{}^{t+\Delta t}\{F\}^{(i)}\right\|} \leq tol_c \tag{2.114}$$

is satisfied. The condensed versions of the vectors ${}^{t+\Delta t}\{\widehat{F}\}, {}^{t+\Delta t}\{\widehat{f}\} and {}^{t+\Delta t}\{\widehat{R}\}$ are obtained from their full versions ${}^{t+\Delta t}\{F\}, {}^{t+\Delta t}\{f\}$ and ${}^{t+\Delta t}\{R\}$ by the expressions similar to equations (2.87) and (2.89). The vector ${}_t\{R\}$ is called as the unbalanced force vector. The right superscript on ${}^{t+\Delta t}\{F\}$ denotes the configuration on which the integration is to be performed to find the external force vector.

As stated in section 2.11.1, the equation of the first Newton-Raphson iteration (i.e. the equation corresponding to ${}_t\{\widehat{R}\}^{(0)} = {}_t\{\Delta\widehat{F}\}$) is solved iteratively using the friction algorithm to determine the status (sticking/slipping) of the interface nodes. Corresponding to this status, further Newton-Raphson iterations are carried out to reduce the magnitude of the unbalanced force vector to zero so as to establish the equilibrium between the external and internal forces.

2.11.3 Arc Length Method

Since the forging problem is a displacement control problem, there is no known external force. Therefore, the denominator in the convergence criterion (2.114) doesn't exist. In that case, one can try to achieve the convergence by making the unbalanced force vector ${}_t\{R\}^{(i)}$ small in an absolute sense. But this slows down the rate of convergence to a considerable extent. To accelerate the rate of convergence, the arc length method is used in conjunction with the modified Newton-Raphson method. In this approach, the unknown nodal reactions at the interface are expressed as a linear combination of a set of known nodal forces. Then the problem is solved as a force control problem using the set of known nodal forces. The unknown coefficients in the linear combination are found from the condition that the vertical component of incremental displacement vector at the interface has a specified value. Since this solution may not satisfy the nodal equilibrium of internal and external forces, iterations need to be performed which are carried out by the modified Newton-Raphson method. Since both the nodal reactions as well as the unbalanced force vector change during an iteration, the incremental equations contain an additional term compared to eq. (2.111).

Originally, the arc length method was proposed only for the case of proportional loading [83,84]. However, in forging problem, the loading is non-proportional. Therefore, the method needs to be modified appropriately to take care of non-proportional loading. The modified method is described in this section.

In i^{ih} iteration, the incremental eq. (2.110) is expressed as[2]

---

[2]In this section, the superscripts/subscripts denoting time have been omitted for the sake of convenience.

$$[\widehat{K}]\{\Delta\widehat{u}\}^{(i)} = \{\Delta\widehat{F}\}^{(i)} + \{\widehat{R}\}^{(i-1)} \tag{2.115}$$

where $\{\widehat{R}\}^{(i-1)}$ is the unbalanced force vector given by

$$\{\widehat{R}\}^{(i-1)} = \{\widehat{F}\}^{(i-1)} - \{\widehat{f}\}^{(i-1)} \tag{2.116}$$

and the incremental force vector $\{\Delta\widehat{F}\}^{(i)}$ is expressed as

$$\{\Delta\widehat{F}\}^{(i)} = \sum_{k=1}^{m} (\Delta\lambda)_k^i \{P\}_k \tag{2.117}$$

Here, m is the number of nodes at the interface and $\{P\}_k$ is a known nodal force vector corresponding to a unit (vertically downward) point force at node k. The vectors $\{P\}_k$, $k = 1, m$ are called as the basic load vectors. The coefficients $(\Delta\lambda)_k^{(i)}$ are unknowns.

Since equation (2.115) is a linear equation, one can decompose the solution as

$$\{\Delta\widehat{u}\}^{(i)} = \sum_{k=1}^{m} (\Delta\lambda)_k^i \{\Delta u^{(k)I}\} + \{\Delta u^{II}\}^{(i)} \tag{2.118}$$

where $\{\Delta u^{(k)I}\}$ and $\{\Delta u^{II}\}^{(i)}$ are obtained as solutions of the following problems:

$$[\widehat{K}]\{\Delta u^{(k)I}\} = \{P\}_k, \ k = 1, m, \tag{2.119}$$

$$[\widehat{K}]\{\Delta u^{II}\}^{(i)} = \{\widehat{R}\}^{(i-1)} \tag{2.120}$$

Thus, $\{\Delta u^{(k)I}\}$ represents the iterative displacement vector due to the basic load vector at node k and $\{\Delta u^{II}\}^{(i)}$ represents the iterative displacement vector due to the unbalanced force vector $\{\widehat{R}\}^{(i-1)}$.

To find the complete solution of (2.115), one needs to determine $(\Delta\lambda)_k^{(i)}$, $k = 1, m$. They are determined from the following condition. At the nodes on the interface, the vertical or z-component of the incremental displacement vector is known. Thus, for nodes $l = 1, m$:

$$\sum_{k=1}^{m} (\Delta\lambda)_k^{(i)} \Delta u_{lz}^{(k)I} + \Delta u_{lz}^{(i)II} = \text{specified value} \tag{2.121}$$

These are m equations in m unknowns: $(\Delta\lambda)_k^{(i)}, k = 1, m$. By solving these equations, the unknown $(\Delta\lambda)_k^{(i)}$ are calculated. Then the iterative displacements are determined from eq (2.118). These displacements are used to find the internal force vector $\{\widehat{f}\}^{(i)}$. Finally, the external force vector at the end (of ith) iteration is found from

$$\{\widehat{F}\}^{(i)} = \{\widehat{F}\}^{(i-1)} + \sum_{k=1}^{m} (\Delta\lambda)_k^i \{P\}_k \tag{2.122}$$

This force vector is used to find the unbalanced force vector and then to check the convergence using eq. (2.114).

While solving eq (2.119,2.120), the upper triangularization of the coefficient matrix $[\widehat{K}]$ needs to be done only once. Then, one can use the resolving facility first to perform the Gauss elimination operations on different right side vectors and then to find $\{\Delta u^{(k)I}\}$ and $\{\Delta u^{II}\}^{(i)}$ by back substitution.

Equation (2.121) takes a different form for the first iteration than for other iterations. These forms are as follows:

First iteration:

for the first iteration, $_t\{\widehat{R}\}^{(0)} = \{0\}$ implies that $\{\Delta u^{II}\}^{(i)} = \{0\}$. Thus, eq (2.121) becomes

$$\sum_{k=1}^{m}(\Delta\lambda)_k^{(i)}\Delta u_{lz}^{(k)I} = \text{specified value} \tag{2.123}$$

Subsequent iterations:

Since the value of specified incremental displacement does not change during an iteration cycle, in subsequent iterations, the right side of eq. (2.121) becomes zero. Thus,

$$\sum_{k=1}^{m}(\Delta\lambda)_k^{(i)}\Delta u_{lz}^{(k)I} + \Delta u_{lz}^{(i)II} = 0 \quad i \geq 2 \tag{2.124}$$

2.11.4   Numerical Integration Scheme

Exact evaluation of integrals appearing in element coefficient matrices and right side vectors is not always possible because of the complexity of the integrands. In such cases, it is natural to seek numerical evaluation of these integral expressions. Numerical integration involves approximation of the integrand by a polynomial of appropriate degree, because the integral of a polynomial can be evaluated exactly.

The most commonly used numerical integration method is Gauss-Legendre integration method. The expression for the integral over a master element Ω_R is given by

$$\int_{\Omega_R} F(\xi,\eta)d\xi, d\eta = \int_{-1}^{+1}\int_{-1}^{+1}F(\xi,\eta)d\xi, d\eta$$

$$\simeq \sum_{i=1}^{m}\sum_{j=1}^{n}F(\xi_i,\eta_j)\omega_i\omega_j \tag{2.125}$$

2.11.5   Divergence Handling Procedures

The modified Newton-Raphson method diverges in some cases. The following simple but fairly effective techniques, for overcoming the divergence are incorporated in the present work.

1. Under-relaxation: The iterative displacement is scaled by a factor α_u ($0 < \alpha_u < 1$). Thus, the iterative displacement vector is given by

$$_t\{\Delta\hat{u}\}^{(i)} = \alpha_u\{\Delta\hat{u}\}^{(i)} \tag{2.126}$$

where $\{\Delta\hat{u}\}^{(i)}$ is the solution of equation (2.111) and α_u is determined so that the numerical method does not diverge.

2. Line search: In this technique, the displacement vector is updated according to the relation [78]

$$^{t+\Delta t}\{\hat{u}\}^{(i)} = {}^{t+\Delta t}\{\hat{u}\}^{(i-1)} + \alpha_l {}_t\{\Delta\hat{u}\}^{(i)} \tag{2.127}$$

where α_l is determined to minimize the unbalanced force vector.

A full line search is computationally expensive. Therefore a cheaper technique is to evaluate unbalance at n different α_l values and choose that α_l which corresponds to the minimum unbalance. This offers a good compromise between computational effort spent in line search and effort saved due to convergence in reduced number of iterations.

3. Incremental displacement cutting: In case the above two procedures fail, incremental displacement cutting is performed.

Chapter 3

Results and Discussion

The finite element model of axisymmetric forging process developed in the previous chapter has been applied to a number of cases involving various sets of input variables.

. In this chapter, the study is performed on a cylindrical disc. Only upper half of the disc is considered for analysis due to symmetry of the geometry and boundary conditions. The convergence study is carried out for Dhar's [46,75] damage variable D and stresses with mesh sizes 3x3, 6x6 and 12x12. Two increment sizes 0.1 mm and 0.05 mm are used in the convergence study. In section 3.1, some typical results are presented where growth of D is discussed along with the hydrostatic stress, circumferential stress σ_θ and axial stress σ_z distributions. In the last section, the parametric study is carried out to show the effects of various input variables. A comparison of bulged profiles is also presented.

3.1 Typical Results

In this section, the distribution of Dhar's damage variable D is closely studied for a typical set of input variables. The material properties, friction coefficient and blank size used in this study are as follows:

Material Properties
Material: Steel SAE 1090,
Modulus of Elasticity $E = 210$ GPa,
Poisson's ratio $\nu = 0.3$,
Initial yield stress $(\sigma_y)_0 = 464.00$ MPa,
Hardening coefficient $K = 1115.00$,
Hardening Exponent $n = 0.19$;
Friction Coefficient:
$\mu = 0.05$;

Blank Size:

Height (H) = 10 mm.

Diameter (ϕ) = 10 mm:

Constants for Dhar's criterion [46,75]:

$C_D = 1.898 \times 10^{-2}$,

$a_1 = 9.8 \times 10^{-4}$ MPa^{-1} ,

$a_2 = 1.84$ MPa^{-1}.

Critical damage value $D_c = 0.05$.

A 12x12 elements nonuniform mesh is used and step size taken is 0.05 mm. Three different reductions are considered, when the damage variable D reaches the critical value of 0.05 at (I) the die-workpiece interface near the free surface of the cylindrical disc, (II) the geometric centre of the disc and (III) the middle of the free surface of disc. These reductions are 25%, 29% and 35% respectively.

Figures 3.1, 3.2 and 3.3 show the damage distribution at these reductions. Analysis of these figures shows that D becomes critical, first at the edge (i.e. at the die-workpiece interface near the free surface), then at the centre of the disc. With further deformation, D grows radially outwards and then reaches the critical value at the meridian surface (the middle of the free surface). By this reduction, D is above 0.05 everywhere in the domain except the centre of flat surface of the disc. Equivalent strain distribution at 35% reduction is shown in figure 3.4. From this, it is clear that the maximum damage at the edge is due to severe deformation and hence high strains here. On the other hand, the strain values are minimum at the centre of the flat surface. Thus, micro-cracks will first occur at the edge of the disc, then at the centre and finally at the meridian surface. But experimental results [56,57,72,73] show that the fractures are seen at the meridian surface. To understand this, hydrostatic stress, circumferential stress σ_θ and axial stress σ_z distributions are also discussed below.

Figures 3.5, 3.6 and 3.7 show the distributions of hydrostatic stress at different reductions mentioned above. From these figures, it is clear that the hydrostatic pressure (negative hydrostatic stress) is minimum at the meridian surface of the disc, while it is quite higher at the other two locations. Thus, the possibility of a fracture is higher at the meridian surface. As the reduction is increased, the hydrostatic pressure becomes less at the meridian surface, while it increases at the other two locations suppressing the growth of micro-cracks developed there.

Study of the figures 3.8, 3.9 and 3.10 showing the σ_θ distributions at different reductions makes the location of fracture (not micro-cracks) initiation site more clear. It can be seen that σ_θ is tensile at the meridian surface, while it is compressive at the top and at the centre of the disc. With higher reductions, the value of σ_θ becomes more tensile at the meridian surface, while it becomes more compressive at the top and the core of the disc. Thus, micro-cracks

initiated at the meridian surface can grow fast to a fracture.

At these three reductions, distributions of σ_z are also shown (figures 3.11-3.13). The axial stress. σ_z is compressive everywhere in the domain. It is the minimum compressive at the meridian surface and this shows the maximum chance of crack growth here. Unlike σ_θ, σ_z continues to become more compressive everywhere in the domain with increase in reduction.

Figure 3.14 shows bulge profiles at the three reductions presented above. The bulging is more at higher reduction.

3.2 Parametric Studies

In this, section effects of the coefficient of friction and height to diameter ratio on micro-cracks occurrence are studied. The nonuniform mesh with 144 elements (12x12) and the increment size of 0.05 mm are used, which are same as used in the previous section. The material is also the same (SAE 1090 steel). The size of the blank is such that its volume is equal to that of the blank of height (H) and diameter (ϕ) equal to 10 mm each which has been used earlier.

3.2.1 Effect of Coefficient of Friction

The analysis is carried out for the coefficient of friction $\mu = 0.1$ and then results are compared with that for $\mu = 0.05$ described earlier. The analysis is carried out for H/ϕ ratio equal to 1 ($H = \phi = 10$ mm) and for three distinguished reductions as mentioned earlier.

These reductions in this case are found to be 20%, 25% and 35% when damage D becomes critical at the edge, at the centre and at the meridian surface of the disc respectively. A worth mentioning point in this case is that D becomes critical at 20% reduction only, while with $\mu = 0.05$, this was at 25% reduction. Thus, with higher friction, micro-cracks initiate at less reduction along the die-workpiece interface near the free surface.

Figures 3.15-3.17 show the growth of D with increasing reduction and the trend is same as discussed in the previous section (3.1). Thus micro-cracks first initiate at the edge of disc, then at the centre and finally at the meridian surface. At these three reductions, hydrostatic stress, σ_θ and σ_z distributions are also presented in figures 3.18-3.26. Again the pattern is the same as discussed in section 3.1. Hydrostatic stress and σ_z are the least compressive and σ_θ is the maximum tensile at the meridian surface. At higher reduction, hydrostatic pressure becomes more everywhere except the meridian surface where it turns less. The circumferential stress σ_θ becomes more tensile and the axial stress σ_z, less compressive at this location. Here, therefore, micro-cracks will grow faster and fracture will occur first.

Figures 3.3 and 3.17 can be compared for damage at different friction levels. It can be noted that the damage D increases everywhere in the domain except the region near the centre of the flat face of the disc when the friction is increased. With $\mu = 0.1$, σ_z becomes more compressive everywhere except the region near the meridian surface where it turns less

compressive; while σ_θ becomes more compressive at the edge and at the core of the disc and, more tensile at the meridian surface. At higher friction, the hydrostatic pressure increases everywhere except the meridian surface where it reduces and becomes nearly zero. This shows that the fracture occurs at less reduction with higher friction.

Figure 3.27 shows the bulge profiles for $\mu = 0.05$ and $\mu = 0.1$, at 35% reduction. The bulge is severe with higher friction due to higher resistance to material movement along the die-workpiece interface.

3.2.2 Effect of Height to Diameter Ratio (H/ϕ Ratio)

The effect of height to diameter ratio (H/ϕ ratio) is studied by carrying out the analysis for the following three cases: (I) $H/\phi =0.5$, (II) $H/\phi =1$, (III) $H/\phi =2$. While varying the H/ϕ ratio, the volume of the blank is kept constant. The analysis is carried out for the coefficient of friction $\mu =0.05$. Three typical reductions are considered when the damage D reaches the critical value at three locations in the disc: the edge, centre and meridian surface respectively.

These reductions are found to be 27.2%, 28.8% and 31.9% for $H/\phi =0.5$; 25.0%, 29.0% and 35.0% for $H/\phi =1$ and 27.3%, 30.4% and 32.9% for $H/\phi =2$. This shows that the micro-cracks initiate at less reduction in case of $H/\phi =1$. Damage D, hydrostatic stress, σ_θ and σ_z distributions for $H/\phi =0.5$ are shown in figures 3.28-3.39, and for $H/\phi =2$, in figures 3.40-3.51. These distributions for $H/\phi =1$ are already shown in figures 3.1-3.3 and 3.5-3.13. For a particular H/ϕ ratio, the pattern of these distributions and their variation when reduction is increased is the same as discussed in section 3.1.

The cases for various H/ϕ ratios when D is 0.05 near the origin (disc-centre) are considered next. Figures 3.32, 3.6 and 3.44 show that the hydrostatic pressure, σ_θ and σ_z at the centre of the disc become less compressive with increasing H/ϕ ratio. Thus, it can be said that the possibility of formation of a central cavity is more with the higher H/ϕ ratio.

Comparison of figures 3.33, 3.7 and 3.45 (when the damage D has reached 0.05 at the meridian surface) show that in case of $H/\phi =1$, the hydrostatic pressure at the meridian surface is less than that in case of $H/\phi =0.5$ or $H/\phi =2$. Similarly, figures 3.36, 3.10 and 3.48 show that σ_θ is the maximum tensile for $H/\phi =1$. Thus meridian surface fracture will appear at less reduction for $H/\phi =1$. This is in agreement with the work of Clift et al. [65].
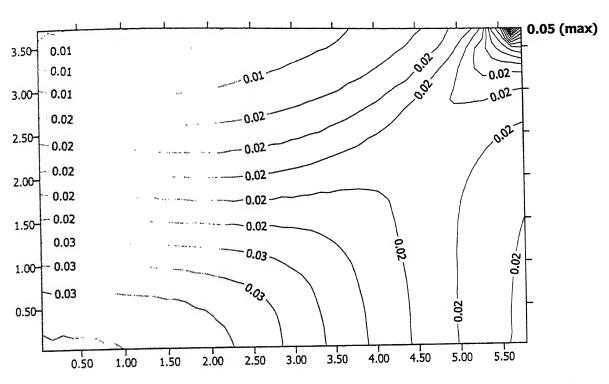
Figure 3.1: Damage 'D' Distribution. (Reduction=25.0%, μ=0.05, H/ϕ=1, H=10.0 mm, ϕ=10.0 mm, Mesh Size=12x12, Increment size=0.05 mm, AISI −1090 steel)
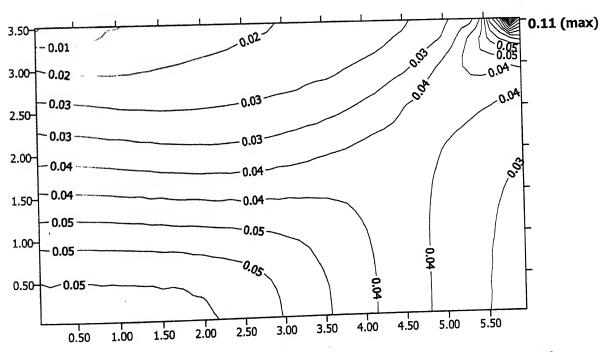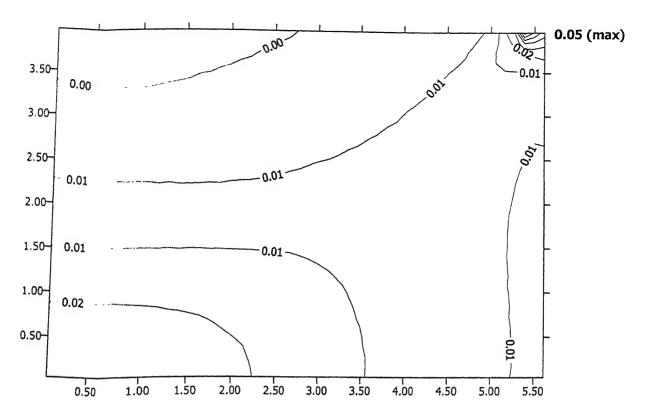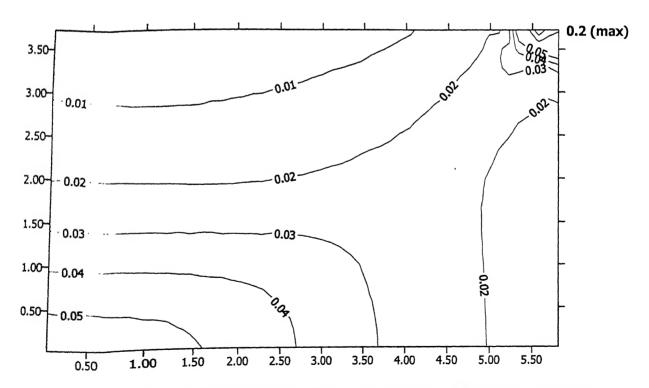

Figure 3.2: Damage 'D' Distribution. (Reduction=29.0%, μ=0.05, H/ϕ=1, H=10.0 mm, ϕ=10.0 mm, Mesh Size=12x12, Increment size=0.05 mm, AISI −1090 steel)
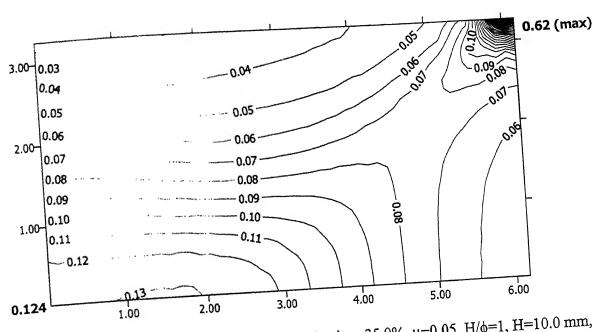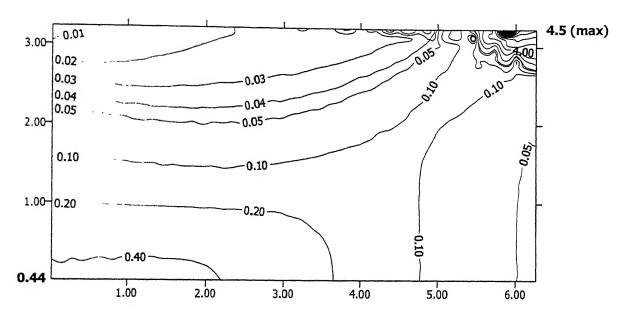
Figure 3.3:   Damage 'D' Distribution. (Reduction=35.0%, μ=0.05, H/φ=1, H=10.0 mm, φ=10.0 mm, Mesh Size=12x12, Increment size=0.05 mm, AISI –1090 steel)
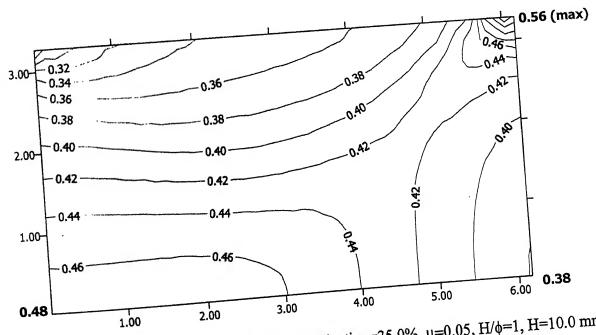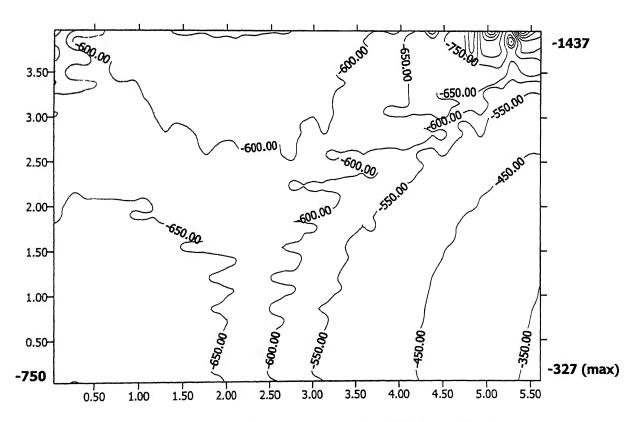

Figure 3.4:   Equivalent Strain Distribution. (Reduction=35.0%, μ=0.05, H/φ=1, H=10.0 mm, φ=10.0 mm, Mesh Size=12x12, Increment size=0.05 mm, AISI –1090 steel)
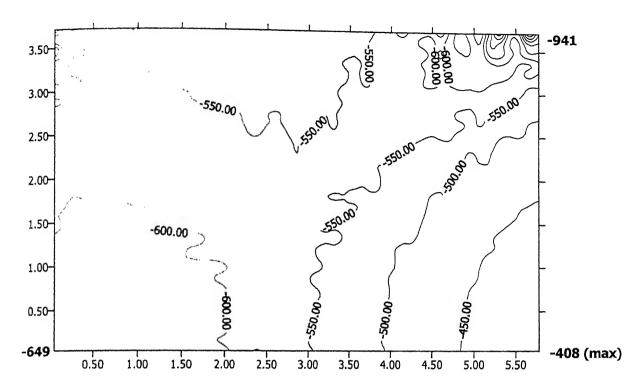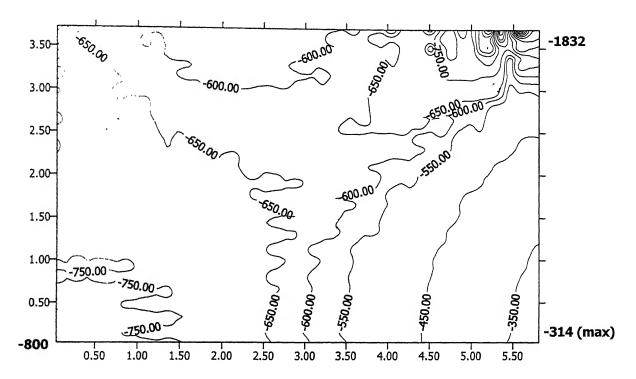
Figure 3.5: Hydrostatic Stress Distribution (in MPa). (Reduction=25.0%, μ=0.05, H/ϕ=1, H=10.0 mm, ϕ=10.0 mm, Mesh Size=12x12, Increment size=0.05 mm, AISI –1090 steel)
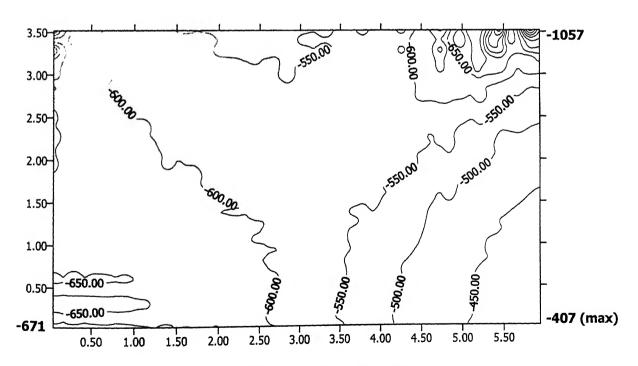
Figure 3.6: Hydrostatic Stress Distribution (in MPa). (Reduction=29.0%, μ=0.05, H/ϕ=1, H=10.0 mm, ϕ=10.0 mm, Mesh Size=12x12, Increment size=0.05 mm, AISI –1090 steel)
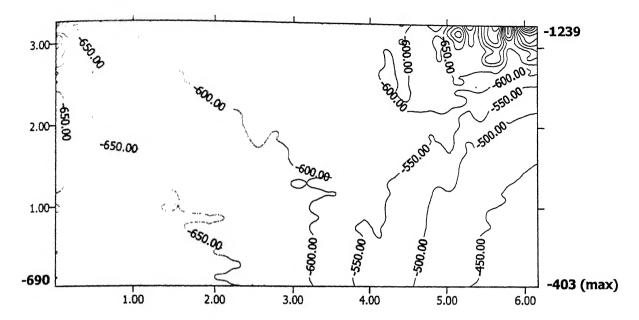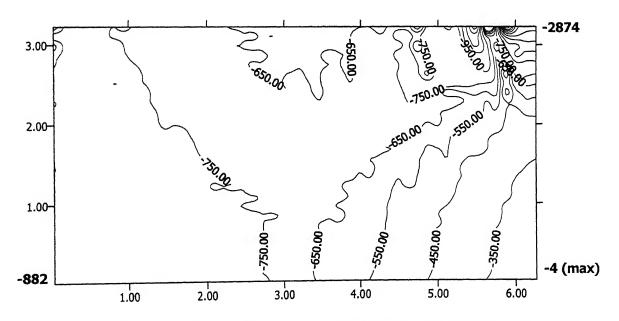
Figure 3.7: Hydrostatic Stress Distribution (in MPa). (Reduction=35.0%, μ=0.05, H/ϕ=1, H=10.0 mm, ϕ=10.0 mm, Mesh Size=12x12, Increment size=0.05 mm, AISI –1090 steel)
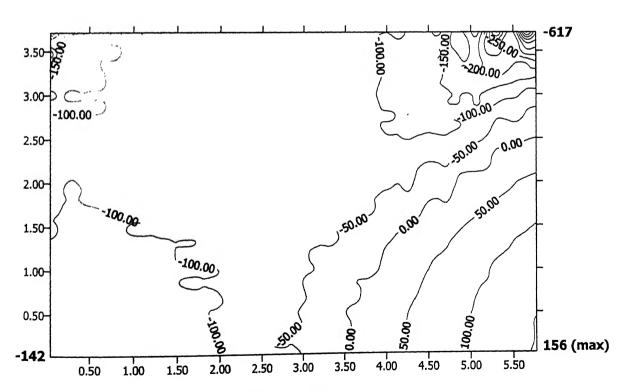
Figure 3.8: σ_θ Distribution (in MPa). (Reduction=25.0%, μ=0.05, H/ϕ=1, H=10.0 mm, ϕ=10.0 mm, Mesh Size=12x12, Increment size=0.05 mm, AISI –1090 steel)
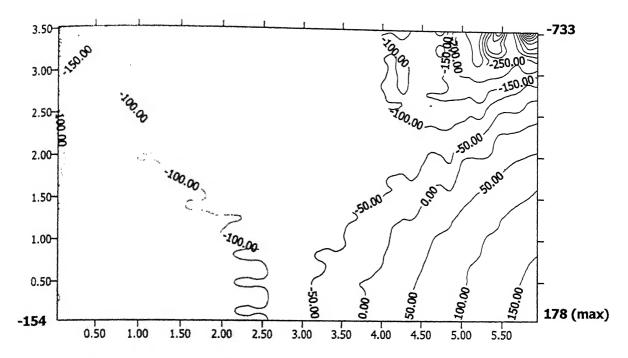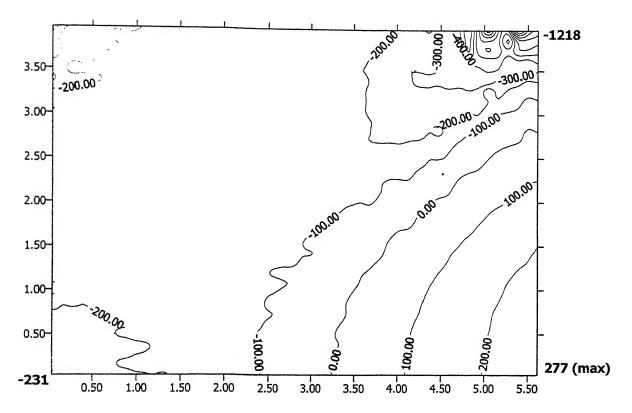
Figure 3.9: σ_θ Distribution (in MPa). (Reduction=29.0%, μ=0.05, H/φ=1, H=10.0 mm, φ=10.0 mm, Mesh Size=12x12, Increment size=0.05 mm, AISI –1090 steel)
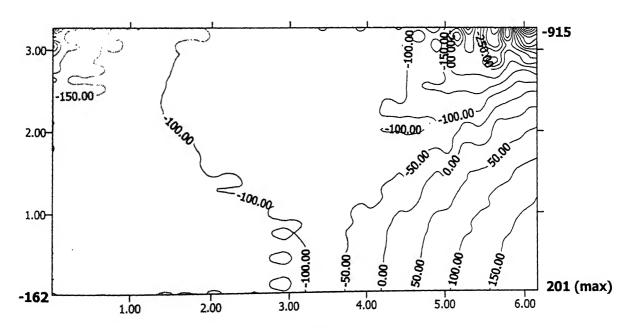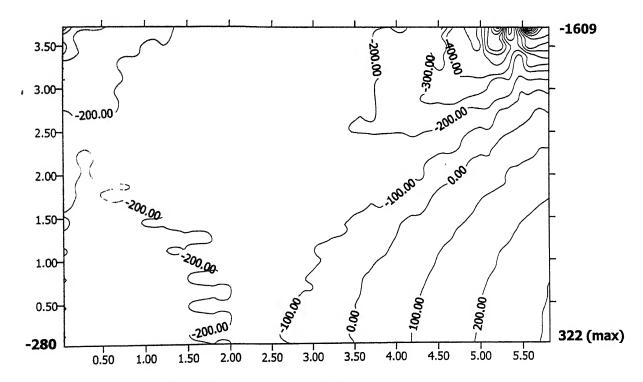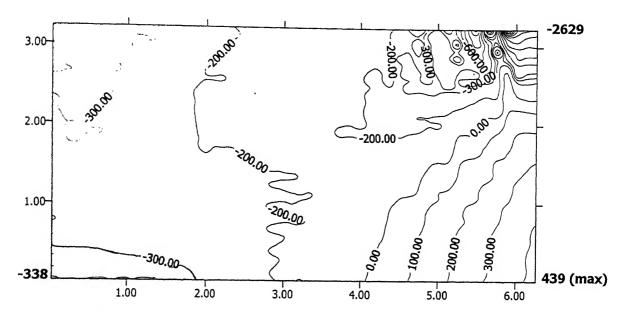

Figure 3.10: σ_θ Distribution (in MPa). (Reduction=35.0%, μ=0.05, H/φ=1, H=10.0 mm, φ=10.0 mm, Mesh Size=12x12, Increment size=0.05 mm, AISI –1090 steel)
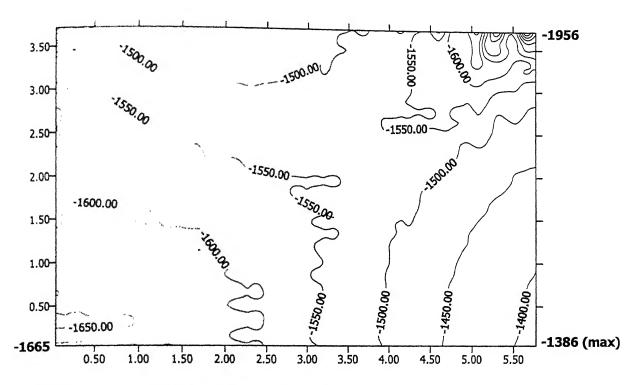
Figure 3.11: σ_z Distribution (in MPa). (Reduction=25.0%, μ=0.05, H/φ=1, H=10.0 mm, φ=10.0 mm, Mesh Size=12x12, Increment size=0.05 mm, AISI −1090 steel)
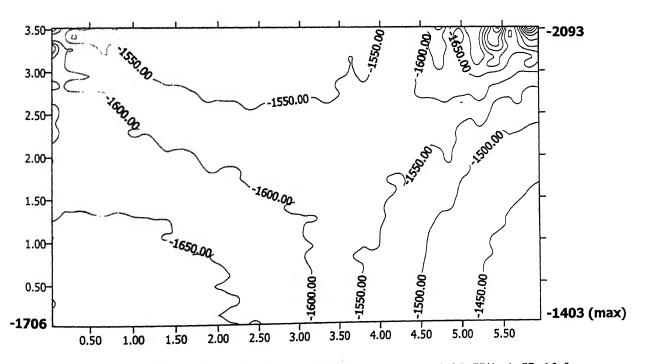
Figure 3.12: σ_z Distribution (in MPa). (Reduction=29.0%, μ=0.05, H/φ=1, H=10.0 mm, φ=10.0 mm, Mesh Size=12x12, Increment size=0.05 mm, AISI −1090 steel)
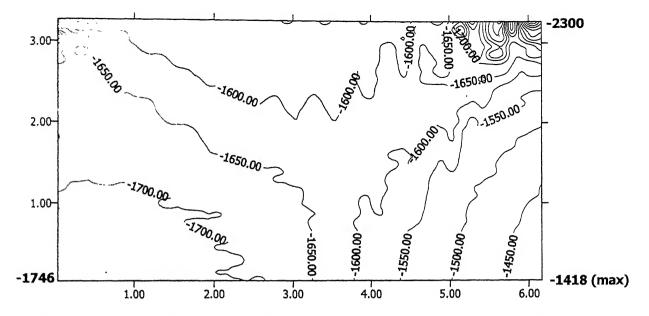
Figure 3.13: σ_z Distribution (in MPa). (Reduction=35.0%, μ=0.05, H/ϕ=1, H=10.0 mm, ϕ=10.0 mm, Mesh Size=12x12, Increment size=0.05 mm, AISI –1090 steel)
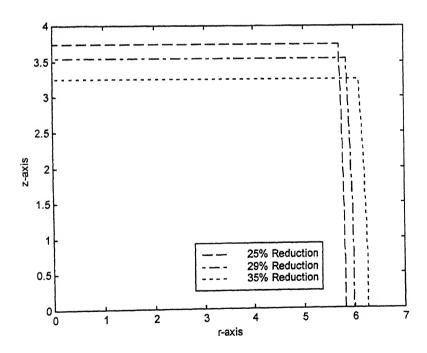
Figure 3.14:   Bulge Profiles at Different Reductions (μ=0.05, H/ϕ=1, H=10.0 mm, ϕ=10.0 mm, Mesh Size=12x12, Increment size=0.05 mm, AISI –1090 steel)

Figure 3.15:   Damage 'D' Distribution. (Reduction=20.0%, μ=0.1, H/φ=1, H=10.0 mm, φ=10.0 mm, Mesh Size=12x12, Increment size=0.05 mm, AISI –1090 steel)
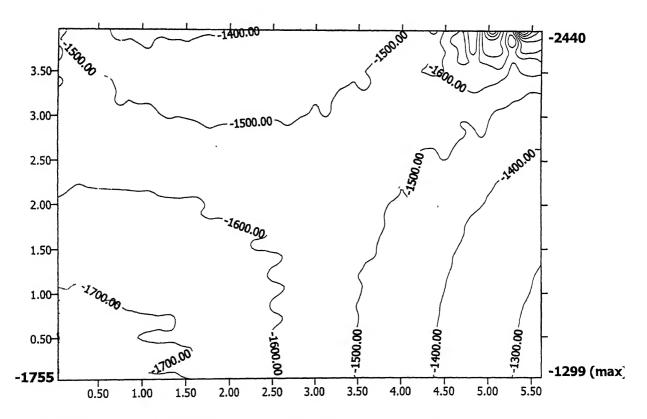

Figure 3.16:   Damage 'D' Distribution. (Reduction=25.0%, μ=0.1, H/φ=1, H=10.0 mm, φ=10.0 mm, Mesh Size=12x12, Increment size=0.05 mm, AISI –1090 steel)

Figure 3.17:   Damage 'D' Distribution. (Reduction=35.0%, μ=0.1, H/φ=1, H=10.0 mm, φ=10.0 mm, Mesh Size=12x12, Increment size=0.05 mm, AISI –1090 steel)

Figure 3.18:   Hydrostatic Stress Distribution (in MPa). (Reduction=20.0%, μ=0.1, H/φ=1, H=10.0 mm, φ=10.0 mm, Mesh Size=12x12, Increment size=0.05 mm, AISI –1090 steel)

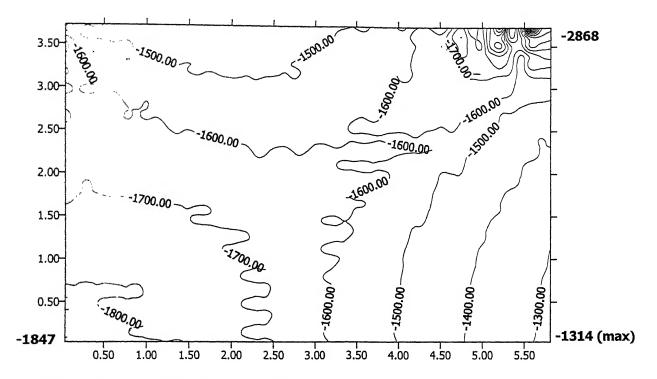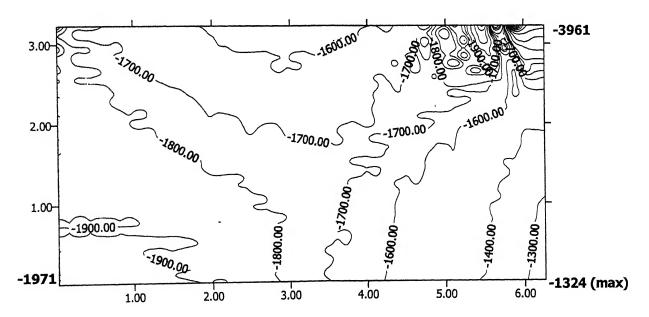Figure 3.19:   Hydrostatic Stress Distribution (in MPa). (Reduction=25.0%, μ=0.1, H/φ=1, H=10.0 mm, φ=10.0 mm, Mesh Size=12x12, Increment size=0.05 mm, AISI –1090 steel)
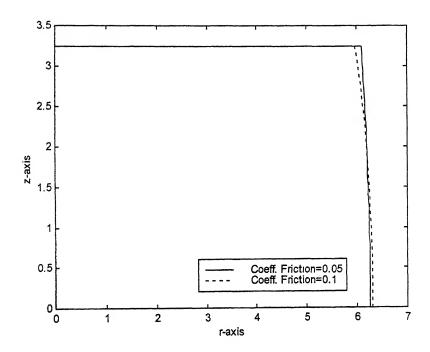

Figure 3.20:   Hydrostatic Stress Distribution (in MPa). (Reduction=35.0%, μ=0.1, H/φ=1, H=10.0 mm, φ=10.0 mm, Mesh Size=12x12, Increment size=0.05 mm, AISI –1090 steel)

Figure 3.21: σ_θ Distribution (in MPa). (Reduction=20.0%, μ=0.1, H/ϕ=1, H=10.0 mm, ϕ=10.0 mm, Mesh Size=12x12, Increment size=0.05 mm, AISI –1090 steel)

Figure 3.22: σ_θ Distribution (in MPa). (Reduction=25.0%, μ=0.1, H/ϕ=1, H=10.0 mm, ϕ=10.0 mm, Mesh Size=12x12, Increment size=0.05 mm, AISI –1090 steel)

Figure 3.23: σ_θ Distribution (in MPa). (Reduction=35.0%, μ=0.1, H/ϕ=1, H=10.0 mm, ϕ=10.0 mm, Mesh Size=12x12, Increment size=0.05 mm, AISI −1090 steel)

Figure 3.24: σ_z Distribution (in MPa). (Reduction=20.0%, μ=0.1, H/ϕ=1, H=10.0 mm, ϕ=10.0 mm, Mesh Size=12x12, Increment size=0.05 mm, AISI −1090 steel)

Figure 3.25: σ_z Distribution (in MPa). (Reduction=25.0%, μ=0.1, H/ϕ=1, H=10.0 mm, ϕ=10.0 mm, Mesh Size=12x12, Increment size=0.05 mm, AISI −1090 steel)

Figure 3.26: σ_z Distribution (in MPa). (Reduction=35.0%, μ=0.1, H/ϕ=1, H=10.0 mm, ϕ=10.0 mm, Mesh Size=12x12, Increment size=0.05 mm, AISI −1090 steel)

Figure 3.27:   Bulge Profiles at Different Friction Levels.
(Reduction=35.0%, H/ϕ=1, H=10.0 mm, ϕ=10.0 mm, Mesh Size=12x12,
Increment size=0.05 mm, AISI –1090 steel)
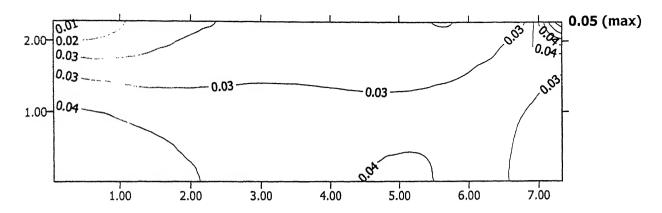
Figure 3.28:   Damage 'D' Distribution. (Reduction=27.2%, μ=0.05, H/φ=0.5, H=6.3 mm, φ=12.6 mm, Mesh Size=12x12, Increment size=0.05 mm, AISI –1090 steel)
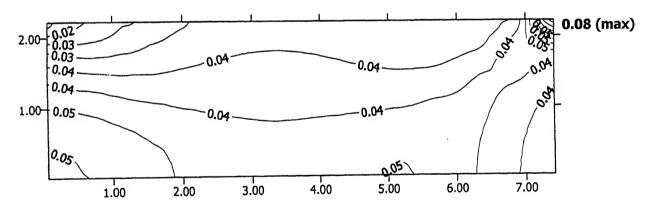
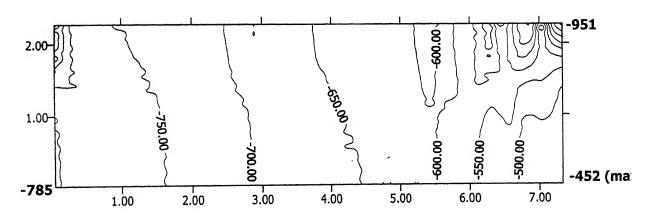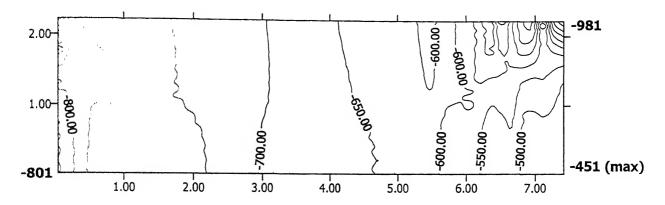

Figure 3.29:   Damage 'D' Distribution. (Reduction=28.8%, μ=0.05, H/φ=0.5, H=6.3 mm, φ=12.6 mm, Mesh Size=12x12, Increment size=0.05 mm, AISI –1090 steel)
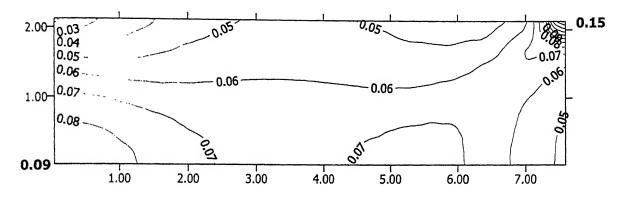
Figure 3.30:   Damage 'D' Distribution. (Reduction=31.9%, μ=0.05, H/φ=0.5, H=6.3 mm, φ=12.6 mm, Mesh Size=12x12, Increment size=0.05 mm, AISI –1090 steel)

Figure 3.31:   Hydrostatic Stress Distribution (in MPa). (Reduction=27.2%, μ=0.05, H/φ=0.5, H=6.3 mm, φ=12.6 mm, Mesh Size=12x12, Increment size=0.05 mm, AISI –1090 steel)

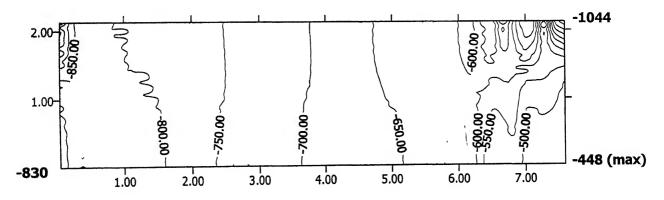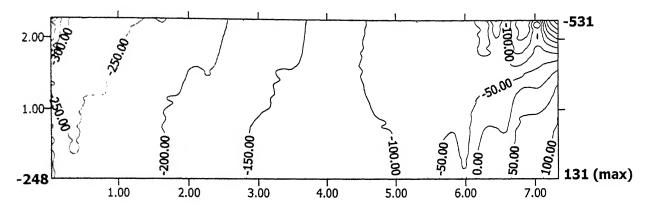Figure 3.32: Hydrostatic Stress Distribution (in MPa). (Reduction=28.8%, μ=0.05, H/ϕ=0.5, H=6.3 mm, ϕ=12.6 mm, Mesh Size=12x12, Increment size=0.05 mm, AISI –1090 steel)

Figure 3.33: Hydrostatic Stress Distribution (in MPa). (Reduction=31.9%, μ=0.05, H/ϕ=0.5, H=6.3 mm, ϕ=12.6 mm, Mesh Size=12x12, Increment size=0.05 mm, AISI –1090 steel)

Figure 3.34: σ_θ Distribution (in MPa). (Reduction=27.2%, μ=0.05, H/ϕ=0.5, H=6.3 mm, ϕ=12.6 mm, Mesh Size=12x12, Increment size=0.05 mm, AISI –1090 steel)
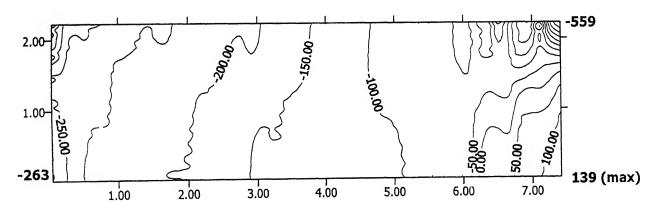

Figure 3.35: σ_θ Distribution (in MPa). (Reduction=28.8%, μ=0.05, H/ϕ=0.5, H=6.3 mm, ϕ=12.6 mm, Mesh Size=12x12, Increment size=0.05 mm, AISI –1090 steel)
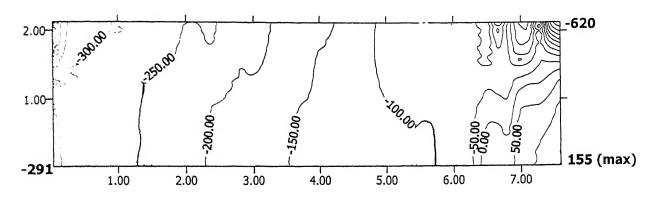
Figure 3.36: σ_θ Distribution (in MPa). (Reduction=31.9%, μ=0.05, H/ϕ=0.5, H=6.3 mm, ϕ=12.6 mm, Mesh Size=12x12, Increment size=0.05 mm, AISI –1090 steel)

Figure 3.37: σ_z Distribution (in MPa). (Reduction=27.2%, μ=0.05, H/ϕ=0.5, H=6.3 mm, ϕ=12.6 mm, Mesh Size=12x12, Increment size=0.05 mm, AISI –1090 steel)

Figure 3.38: σ_z Distribution (in MPa). (Reduction=28.8%, μ=0.05, H/ϕ=0.5, H=6.3 mm, ϕ=12.6 mm, Mesh Size=12x12, Increment size=0.05 mm, AISI −1090 steel)

Figure 3.39: σ_z Distribution (in MPa). (Reduction=31.9%, μ=0.05, H/ϕ=0.5, H=6.3 mm, ϕ=12.6 mm, Mesh Size=12x12, Increment size=0.05 mm, AISI −1090 steel)
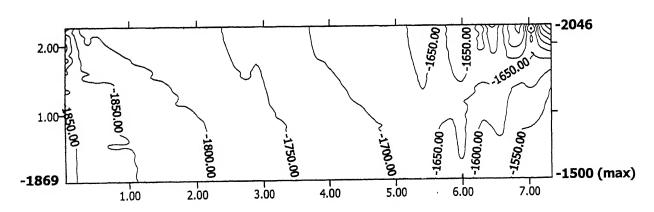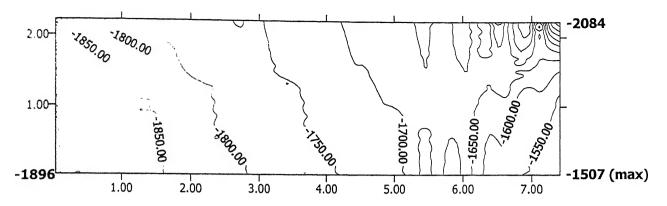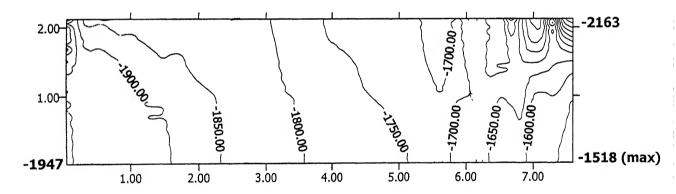
67

Figure 3.40:   Damage 'D' Distribution. (Reduction=27.3%, μ=0.05, H/φ=2, H=15.8 mm, φ=7.9 mm, Mesh Size=12x12, Increment size=0.05 mm, AISI –1090 steel)

Figure 3.41:   Damage 'D' Distribution. (Reduction=30.4%, μ=0.05, H/φ=2, H=15.8 mm, φ=7.9 mm, Mesh Size=12x12, Increment size=0.05 mm, AISI –1090 steel)
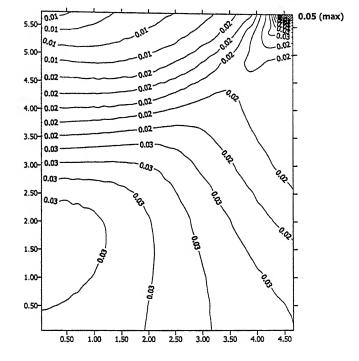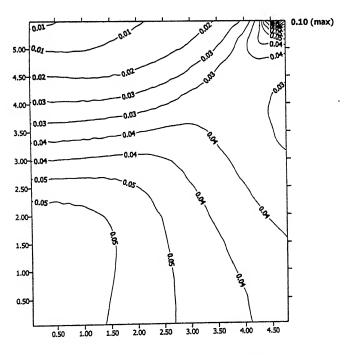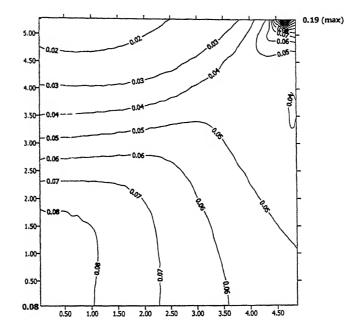
Figure 3.42: Damage 'D' Distribution. (Reduction=32.9%, μ=0.05, H/φ=2, H=15.8 mm, φ=7.9 mm, Mesh Size=12x12, Increment size=0.05 mm, AISI –1090 steel)

Figure 3.43: Hydrostatic Stress Distribution (in MPa). (Reduction=27.3%, μ=0.05, H/φ=2, H=15.8 mm, φ=7.9 mm, Mesh Size=12x12, Increment size=0.05 mm, AISI –1090 steel)

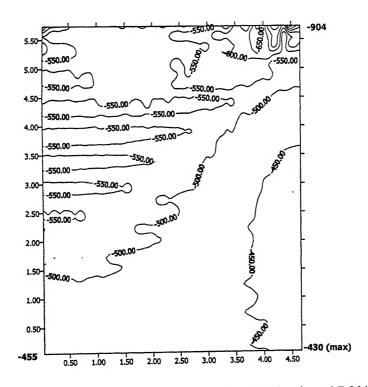Figure 3.44: Hydrostatic Stress Distribution (in MPa). (Reduction=30.4%, μ=0.05, H/φ=2, H=15.8 mm, φ=7.9 mm, Mesh Size=12x12, Increment size=0.05 mm, AISI –1090 steel)
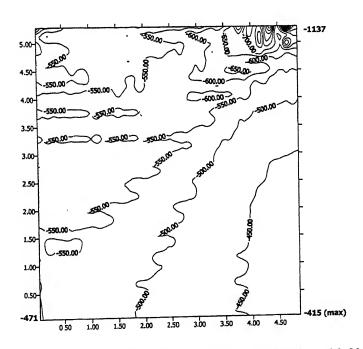
Figure 3.45: Hydrostatic Stress Distribution (in MPa). (Reduction=32.9%, μ=0.05, H/φ=2, H=15.8 mm, φ=7.9 mm, Mesh Size=12x12, Increment size=0.05 mm, AISI –1090 steel)
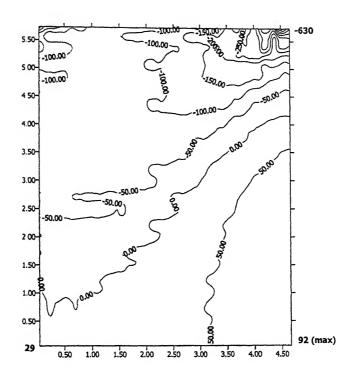
Figure 3.46: σ_θ Distribution (in MPa). (Reduction=27.3%, μ=0.05, H/ϕ=2, H=15.8 mm, ϕ=7.9 mm, Mesh Size=12x12, Increment size=0.05 mm, AISI –1090 steel)
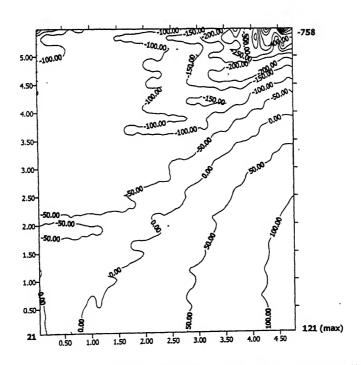
Figure 3.47: σ_θ Distribution (in MPa). (Reduction=30.4%, μ=0.05, H/ϕ=2, H=15.8 mm, ϕ=7.9 mm, Mesh Size=12x12, Increment size=0.05 mm, AISI –1090 steel)
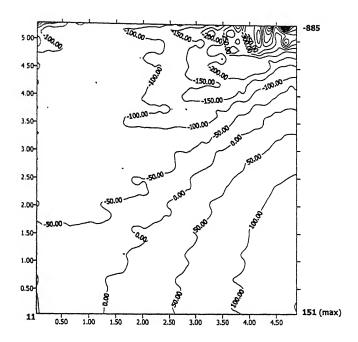
Figure 3.48: σ_θ Distribution (in MPa). (Reduction=32.9%, μ=0.05, H/ϕ=2, H=15.8 mm, ϕ=7.9 mm, Mesh Size=12x12, Increment size=0.05 mm, AISI –1090 steel)

Figure 3.49: σ_z Distribution (in MPa). (Reduction=27.3%, μ=0.05, H/ϕ=2, H=15.8 mm, ϕ=7.9 mm, Mesh Size=12x12, Increment size=0.05 mm, AISI –1090 steel)
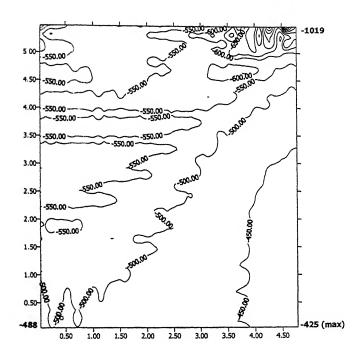
Figure 3.50: σ_z Distribution (in MPa). (Reduction=30.4%, μ=0.05, H/ϕ=2, H=15.8 mm, ϕ=7.9 mm, Mesh Size=12x12, Increment size=0.05 mm, AISI –1090 steel)

Figure 3.51: σ_z Distribution (in MPa). (Reduction=32.9%, μ=0.05, H/ϕ=2, H=15.8 mm, ϕ=7.9 mm, Mesh Size=12x12, Increment size=0.05 mm, AISI –1090 steel)
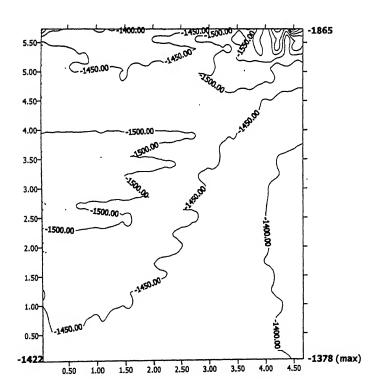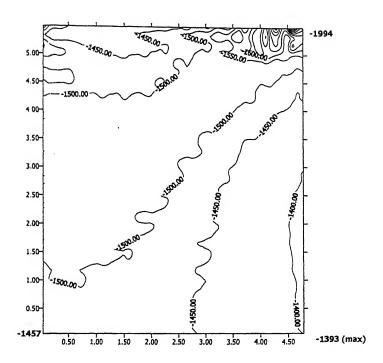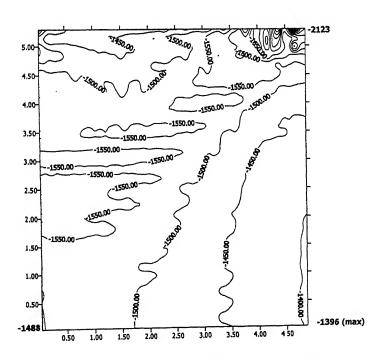
Chapter 4

Conclusions and Scope for Future Work

The objective of this work is to develop an axisymmetric large deformation elasto-plastic finite element code for determination of damage in cold forging process. Coulomb friction model is employed at the die-workpiece interface. The Updated Lagrangian formulation, which is convenient for handling material and geometric non-linearities, is used. New incremental objective stress measure and logarithmic strain measure are used which allow the use of large incremental displacement. Forging process is a displacement-control problem. Therefore, to accelerate the convergence of the iterative solution scheme, arc length method is used in conjunction with the modified Newton Raphson iterative technique. The material is assumed to be elastic-plastic strain hardening and yielding according to the von Mises criterion. The strain hardening behaviour is modelled by a power law. The inertial and body forces are neglected.

Ductile fracture is often a limiting factor in metal forming processes. It is widely known that the ductile fracture is a void nucleation, growth and coalescence phenomenon. A continuum damage mechanics model given by Dhar et al. [46,75] is used for the prediction of defects. For typical values of input variables, the damage, hydrostatic stress, circumferential stress and axial stress distributions are studied. A detailed parametric study of damage is carried out to show the effects of the coefficient of friction at the die-work interface and the height to diameter ratio of the workpiece.

The following conclusions can be drawn from the present study:

- The micro-cracks first initiate along the die-workpiece interface region near the free surface, then at the centre of the workpiece and subsequently at the meridian surface. The amount of damage continues to grow with reduction.

- The fracture will appear first at the meridian surface since the hydrostatic stress and axial stress are the minimum compressive and the circumferential stress is the maximum tensile at this location. Thus, micro-cracks here grow faster to a fracture.

- At higher friction, micro-cracks initiate at less reduction. The meridian surface fracture will also occur early with higher friction since the circumferential stress is more tensile and hydrostatic stress, less compressive at this location. Bulging is more severe when the friction at die-work interface is higher.

- As compared with the case of height to diameter ratio equal to one, blanks with height to diameter ratio less than or greater than unity can sustain more reductions without micro-cracks and fracture. With higher height to diameter ratio, the chances of formation of a central cavity are more because of less compressive hydrostatic stress.

The following points may be considered as an extension of the present study:

- Dependence of material behaviour on strain rate (visco-plasticity) and temperature.

- Analysis and prediction of defects in forging process during unloading and due to residual stresses.

- Determination of the properties for other materials to fit the criterion of void nucleation, growth and coalescence.

- Preprocessor and postprocessor for generation of input data and graphical representation of results.

References

1. Hill, R., Lee, E.H., and Tupper, S.J., 1923, A method of numerical analysis of plastic flow in plane strain and its application to the compression of a ductile material between rough plates, Trans. of ASME, J. Appl. Mech., V-73, p46

2. Green, A.P., 1923, A Theoretical investigation of the compression of ductile material between smooth flat dies, Philosophical Magazine Series 7, V-42, p900.

3. Shabaik, A., Prediction of geometric changes of the free boundary during upsetting by slip line theory, ASME paper no. 70-WA/prd-17.

4. Hoffman, O., Sachs, G., 1953, Introduction to the Theory of Plasticity for Engineers, Mc-Graw Hill Book Company, New York.

5. Altan, T., 1971, Computer simulation to predict load, stress and metal flow in an axisymmetric closed die forging, Metal Forming, ed. Hoffmanner, A.L., Plenum press, p325.

6. Prager, W., and Hodge, P.G., 1951, Theory of Perfectly Plastic Solids, John Wiley, New York.

7. Drucer, P.C., 1954, Coulomb friction, plasticity and limit loads, Trans of ASME, J. Appl. Mech., V-21, p71.

8. Kudo, H., 1960, Some analytical and experimental studies of axisymmetric cold forging and extrusion-I and II, Int. J. Mech. Sci., V-2, p102.

9. Kudo, H., 1960, An upper bound approach to plane strain forging and extrusion-I and II, Int. J. Mech. Sci., V-2, p57.

10. Avitzur, B.,1968, Metal Forming: Processes and Analysis, Mc-Graw Hill Book Company, New York.

11. Kobayashi, S., 1964, Upper bound solution of axisymmetric forming problems, part I and II, Trans of ASME, ser. B, J. Engg. for Ind., V-86, No.-4, p326.

12. MacDonald, A.G., Kobayashi, S., and Thomsen, E.G., 1964, Some problems of press forging lead and aluminum, Trans. of ASME, ser. B, J. Engg. for Ind., V-82, p246.

13. Yang, D.Y., and Kim, J.H.,1987, An analysis of the three dimensional upset forging of regular polygonal blocks by using the upper bound method, Trans. of ASME J. Engg. for Ind., V-109, p155.

14. Kim, J.J., Yang, D.Y., and Kim, M.U., 1987, Analysis of three dimensional upset forging of an arbitrarily shaped prismatic blocks, Int. J. Mach.Tools Manufact, V-27(3), p311.

15. Manuel, J.M., Barata Marques and Paulo A.F. Martins, 1991, The use of dual stream functions in the analysis of three dimensional metal forming processes, Int. J. Mech. Sci., V-33, p313.

16. Lee, C.H., and Kobayashi, S., 1971, Analysis of axisymmetric upsetting and plane strain side pressing of solid cylinders by finite element method, Trans. of ASME, ser. B, J. Engg. for Ind., V-93, p445.

17. Shah, S.N., Lee, C.H., and Kobayashi, S., 1973, Compression of tall, circular, solid cylinders between parallel flat dies, Proc. Int. Conf. Prod. Engr., Tokyo, p295.

18. Chen, C.C., and Kobayashi, S., 1978, Rigid plastic finite element analysis of ring compression: applications to numerical method of forming processes, ASME, AMD, V-28, p163.

19. Oh, S.I., and Kobayashi, S., 1976, Workability of aluminum alloy 7075-t6 in upsetting and rolling, Trans. of ASME, ser. H, J. Engg. for Ind., V-98, p800.

20. Maccarini, G., Pellegrini, C., and Bugini, A., 1991, The influence of die geometry on cold extrusion forging operations: FEM and experimental results, J. Mater. process. Tech., V-27, p227.

21. Hartley, P., Sturgess, C.E.N., Rowe, G.W., 1979, Friction in finite element analysis of metal forming process, Int. J. Mech. Sci., V-21, p301.

22. Hartley, P., Sturgess, C.E.N., Rowe, G.W., 1980, Influence of friction on the prediction of forces, pressures distributions and properties in upset forging, Int. J. Mech. Sci., V-22, p743.

23. Shima, S., Mori, K. and Osakada, K., 1978, Analysis of Metal Forming by the Rigid Plastic Finite Element Method based on Plasticity Theory for Porous Metals, Metal Forming Plasticity, ed Lippmann, H., Springer, p305

24. Pillinger, I., Hartley, P., Sturgess, C.E.N., and Rowe, G.W., 1985, An elastic plastic three dimensional finite element analysis of the upsetting of rectangular blocks and experimental comparison, Int. J. Mach. Tool Des. Res., V-25(3), p229.

25. Bathe, K. J., Ramm, E., and Wilson, E. L., 1975, Finite element formulations for large deformation dynamics analysis, Int. J. Num. Mech. Engg.,V-9, p353.

26. Dadras, P. and Thomas, J.F. Jr, 1983, Analysis of axisymmetric upsetting based on flow pattern observation, Int. J. Mech. Sci., V-25, p421

27. Carter, W.T., Jr and Lee, D., 1986, Further analysis of axisymmetric upsetting, Trans. of ASME, ser. B, J. Engg. for Ind., V-108, p198.

28. Michel B. and Boyer J.C., 1995, Elasto-Visco-Plastic Finite Element Analysis of Cold Upsetting Test, J. Mater. Proc. Tech., V-54, p120.

29. Lin, S.Y., 1995, An Investigation of Die-workpiece Interface Friction during the Upsetting Process, J. Mater. Proc. Tech., V-54, p239.

30. Yang, Q., Qu, S., Zhu, Q. and Min, N., 1997, FE Simulation Method for Forging System, J. Mater. Proc. Tech, V-63, p678.

31. Joun, M.S., Lee, S.W. and Chung, J.H., 1998, Finite Element Analysis of Multistage axisymmetric Forging Process, Int. J. Mach. Tools Manufact., V-38, p843

32. Liou, J.H., and Jang,D.Y., 1997, Forging parameter optimization considering stress distributions in products through FEM analysis and robust design methodology, Int.J. Mach. Tools Manufact, V-37(6), p775.

33. Satyanarayan, V., 1997, Dynamic large deformation elasto plastic analysis of continua, M.Tech. Thesis, Dept. of Mech. Engg., I.I.T.Kanpur (India).

34. Gurson, A.L.,1977, Continuum Theory of Ductile Rupture by Void Nucleation and Growth Part 1 -Yield Criteria and Flow Rules for Porous Ductile Media, ASME J. of Engg. Mat. Tech., V-99, p2.

35. Tvergaard, V., 1981, Influence of Voids on Shear Band Instabilities Under Plane Strain Conditions, Int. J. of Fracture, 17, p389.

36. Needleman, A., and Tvergaard, V., 1984, An Analysis of Ductile Rupture in Notched Bars, J. of Mech. and Phys. of Solids, 32, p461.

37. Oyane, M., 1972, Criteria of Ductile Strain, Bulletin of JSME, 15, p1507.

38. Oyane, M., Sato, T., Okimoto, K., and Shima, S., 1980, Criteria for Ductile Fracture and their Applications, J. of Mech. Work. Tech., 4, p65.

39. Goods, S.H., and Brown, C. M., 1979, The Nucleation of Cavities by Plastic Deformation, Acta Metallurgica, 27, p1.

40. McClintock, F. A., 1968, A Criterion for Ductile Fracture by the Growth of Holes ,ASME J. of App. Mech., 90, p363.

41. Rice, J.R., and Tracey, D.M., 1969, On the Ductile Enlargement of voids in Triaxial Stress Field, J. of Mech. and Phys. of Solids, 17, p201.

42. Argon, A.S., and Im, J., 1975, Separation of Second Phase Particles in Spherodised 1045 Steel, Cu 0.6, Pct Cr Alloy and Maraging Steel in Plastic Straining, Metallurgical Trans. -A, 6, p839.

43. Gurland, J., 1972, Observation on the Fracture of Cementite Particles in Spheroidised 1.05% C Steel Deformed at Room Temperature, Acta Metallurgica, 20, p735.

44. Dung, N.L., 1992, Three Dimensional Void Growth in Plastic Materials, Mechanics Research Communications, 19, p227.

45. Dung, N.L., 1992, Prediction of Void Growth in Tensile Test, Mechanics Research Communications, 19, p341.

46. Dhar, S., 1995, A Continuum Damage Mechanics Model for Ductile fracture, Ph.D. Thesis, Indian Institute of Technology-Kanpur, (India).

47. Lemaitre, J., 1985, A Continuous Damage Mechanics Model for Ductile Fracture, ASME J. of Engg. Mat. and Tech., 107, p83.

48. Le Roy, G., Embury, J.D., Edward, G., and Ashby, M.F., 1981, A Model of Ductile Fracture Based on the Nucleation and Growth of Voids, Acta Metallurgica, 29, p1509.

49. Bridgman, P.W., 1964, Studies in Large Plastic Flow and Fracture, Harvard University Press.

50. Freudenthal, A.M., 1950, The Inelastic Behaviour of Solids, John Wiley.

51. Cockcroft, M. G., and Latham, D.J., 1968, Ductility and the Workability of Metals, J. of the Institute of Metals, 96, p33.

52. Osakada, K., Mori, K., 1978, Prediction of Ductile Fracture in Cold Forging Annals of the CIRP, 27, p135.

53. Norris, D.M., Reaugh, J.E., Moran, B., and Quinnones, D. F., 1978, A Plastic Strain Mean Stress criterion for Ductile Fracture, ASME J. of Engg. Mat. Tech, 100, p279.

54. Al-Mousawi, M.M., Daragheh, A.M. and Ghosh, S.K., 1995, A Database for some Physical Defects in Metal Forming Processes, Material Processing Defects (Ed. Ghosh, S.K. and Predeleanu, M.), Elsevier, p387.

55. Thomason, P.F., 1969, Tensile Plastic Instability and Ductile Fracture Criteria in Uniaxial Compression Tests, Int. J. Mech. Sci., V-11, p187.

56. Kobayashi, S., 1970, Deformation Characteristics and Ductile Fracture of 1040 Steel in Simple Upsetting of Solid Cylinders and Rings, Journal of Engineering for Industry, May, p391.

57. Kuhn, H. A., and Lee., P.W., 1971, Strain Instability and Fracture at the Surface of Upset Cylinders, Metallurgical Transactions, V-2, November, p3197.

58. Hoffmanner, A. L., 1971, Metal Forming Interrelation between Theory and Practice, Plenum press.

59. Johnson, W. and Mamalis, A.G., 1977, A Survey of Some Physical Defects Arising in Metal Working Processes, Proc. 17th Int, MTDR Conf., Macmillan, p607.

60. Sowerby, R. Chandrasekaran, N. Dung, N.L. and Mahrenholtz, 1985, The Prediction of Damage Accumulation during Upsetting Tests Based on McClintock's Model. VDI-Forschung in Ingenieurwesen, p51.

61. Clift, S. E., Hartley, P., Sturgess, C. E. N., and Rowe, G. W.,1985, Fracture Initiation in Plane Strain Forging, Proc. 25th MTDRC, Univ. Birmingham, p413.

62. Dung, N. L., 1986, Fracture Initiation in Upsetting Tests, Proc. of the NUMIFORM'86 Conference, Aug., p261.

63. Predeleanu, M., Cordebois, J. P. and Belkhiri, L., 1986, Failure Analysis of Cold Upsetting by Computer and Experimental Simulation, Proc. of the NUMIFORM'86 Conference, Aug., p277.

64. Mamalis, A. G. and Johnson, W., 1987, Defects in the Processing of Metals and Composites, Computational Methods for Predicting Material Processing Defects (Ed. Predeleanu M.), Elsevier, p231.

65. Clift, S. E., Hartley, P., Sturgess, C. E. N., and Rowe, G. W.,1990, Fracture Prediction in Plastic Deformation Processes, Int. J.Mech. Sci., 32, p1.

66. Johnson, W., 1991, Manufacturing Defects Studies Nothing Some of the Early Ideas of Robert Mallett (1810-1881), Irish Engineer- Scientist, Journal of Materials Processing Technology, 26, p97.

67. Zhu, Y.Y., Cescotto, S., and Habraken, A. M., 1992, A Fully Coupled Elasto-plastic Damage Modeling and Fracture Criteria in Metal forming Processes., J. Mat. Proc. Tech.,32, p 197.

68. Lin, Z. C., and Lin, S. Y., 1993, An investigation of Ductile Fracturing in Mild Steel during Upsetting, Int. J. Mach. Tools Manufact., V-33, No-1, p31.

69. Zhu, Y.Y., Cescotto, S., and Habraken, A. M., 1995, Modeling of Fracture Initiation in Metal Forming Processes, p155.

70. Atkins, A. G., 1996,Fracture in Forming, J. Mat. Proc. Tech., 56, p609.

71. Gouveia, B.P.P.A.A., Rodrigues, J.M.C., Martins, P.A.F., 1996, Fracture Predicting in Bulk Metal Forming., Int.J. Mech. Sci., V-38, No.4, p361.

72. Semiatin, S.L., Goetz, T.L., Shell, E.B., Seetharaman, V. and Ghosh, A.K., 1999, Cavitation and Failure during Hot Forging of Ti-6Al-4V, Metallurgical and Materials Transactions,V-30A, May, p1411.

73. Kim Hong-Seok, Im Yong-Teak and Geiger Manfred., 1999, Prediction of Ductile Fracture in Cold Forging of Aluminum Alloy, Transactions of the ASME, V-121, Aug, p336.

74. Thomason, P.F., 1990, Ductile Fracture of Metals, Pergamon.

75. Dhar, S., Raju Sethuraman, and Dixit, P.M., 1996, A Continuum Damage Mechanics Model for Void Growth and Micro-Crack Initiation, Engg. Fracture Mechanics, V-53, No.-6, p917.

76. Truesdell,C., 1966, The Elements of Continuum Mechanics, Springer Verlag, New York.

77. Dienes, J.K., 1979, On the Analysis of Rotation and Stress Rate in Deforming Bodies, Acta Mechanica, V-32, p217.

78. Crisfield, M.A., 1994, Nonlinear Finite Element Analysis of Solids and Structures, V-1, Essentials, John Wiley and Sons, Chichester.

79. Metzger, D.R., and Dubey, R.B., 1986, Objective Tensor Rates and Frame Indifferent Constitutive Models, Mechanics research Communications, V-13(2), p91.

80. Lee, E.H., 1981, Some Comments on Elastic-Plastic analysis, Int. J. Solid Structures, V-17, p859.

81. Owen, D.R.J. and Hinton. E., 1980, Finite Elements in Plasticity: Theory and Practice, Pineridge Press, Swansea, UK.

82. Bathe. K.J., 1998, Finite Element Procedures, Prentice-Hall of India, New Delhi.

83. Haisler. W.E., and Stricklin, J.A., 1977, Displacement Incrementation in Nonlinear Structural Analysis by the Self-Correcting Method., Int. J. Num. Meth. Engg., V-11, p3.

84. Batoz, J.L. and Dhatt, G., 1979, Incremental Displacement Algorithms for Nonlinear Problems, Int. J. Num. Meth. Engg., V-14(2), p1262.

137946